Distributed Collaborative Beamforming Design for Maximized Throughput in Interfered and Scattered Environments

Slim Zaidi, *Student Member, IEEE*, and Sofiène Affes, *Senior Member, IEEE*

***Abstract*—In this paper, we consider a dual-hop communication from a source surrounded by M_I interferences to a receiver, through a wireless network comprised of K independent terminals. In the first time slot, all sources send their signals to the network, whereas in the second time slot, the terminals multiply the received signal by their respective beamforming weights and forward the resulting signals to the receiver. We design these weights so as to minimize the interferences plus noises' powers while maintaining the received power from the source to a constant level. We show, however, that they are intractable in closed form due to the complexity of the polychromatic channels arising from the presence of scattering. By resorting to a two-ray channel approximation proved valid at relatively low angular spread (AS) values, we are able to derive the new optimum weights and prove that they could be locally computed at each terminal, thereby complying with the distributed feature of the network of interest. The so-obtained bichromatic distributed collaborative beamforming (B-DCB) is then analyzed and compared in performance to the monochromatic CB (MCB), whose design does not account for scattering, and the optimal CSI-based CB (OCB). Comparisons are made under both ideal and real-world conditions where we account for implementation errors and the overhead incurred by each CB solution. They reveal that the proposed B-DCB always outperforms MCB in practice; and that it approaches OCB in lightly to moderately scattered environments under ideal conditions and outperforms it under real-world conditions even in highly scattered environments. In such conditions, indeed, the B-DCB operational regions in terms of AS values over, which it is favored against OCB could reach until 50° and hence cover about the entire span of AS values.**

***Index Terms*—Distributed collaborative beamforming, scattering, angular distribution/spread, interference, wireless sensor networks (WSN).**

I. Introduction

AS A STRONG means to establish a reliable communication over long distances while avoiding coding and other high-cost signal processing techniques, beamforming has gained significant interest in the research community [1]–[24]. Using this technique, a multiple-antenna transceiver transmits or receives a message through its K antennas. Each antenna multiplies its signal by a beamforming weight so that all signals are constructively combined at the destination. These weights are properly selected to achieve a specific design objective while satisfying one or several practical constraints. It has been shown that beamforming is able to not only substantially improve the received signal's quality, but also significantly reduce the antennas power consumption [6]–[8]. However, in several real-word scenarios, practical constraints such as size may rule out the use of multiple-antenna units. In such a case, collaborative communication among K small single-antenna battery-powered terminals (sensor nodes, mobile users, relays, etc.), called collaborative beamforming (CB), can alternatively be used to emulate the conventional beamforming [9]–[24]. In fact, CB allows terminals to operate virtually as a single physical entity and, hence, take advantage of beamforming benefits.

The widely used CB solution that is able to handle both scattering and interference, both present in almost all real-world scenarios, is the optimal CSI-based CB (OCB) [1]–[4], [9]. When the latter is implemented in the network, it has been shown that each collaborating terminal's weight then depends not only on that terminal's CSI, but also on the other terminals' CSI [1]–[4], [9]–[11]. Since terminals are very often autonomous and located at different physical locations, they have limited knowledge about each other's CSI. To compute their respective interdependent weights, they have to exchange their local information resulting inevitably in an undesired overhead. The latter increases with the terminals' number K, the interferences' number M_I as well as the channel Doppler frequencies [10], [11]. If one of these parameters is large, this overhead becomes prohibitive and may cause substantial performance degradation and severe terminals' power depletion. This critical impediment motivates further investigation of strategies able to reduce the overhead incurred by OCB.

As such, the optimized CSI or weights' quantization schemes such as the Grassmannian scheme in [25] appear to be efficient strategies to achieve this goal. Nevertheless, the latter usually require a huge codebook that increases the overall cost of the network if integrated at each terminal. Furthermore, the quantization itself introduces errors in weights, thereby causing a CB's performance degradation. More importantly, such schemes do not significantly reduce overhead since the latter still keeps increasing with K, M_I, and channel Doppler frequencies. Another strategy to circumvent this problem consists in ignoring scattering and assuming instead monochromatic

Manuscript received February 13, 2015; revised July 31, 2015 and September 21, 2015; accepted October 6, 2015. Date of publication October 27, 2015; date of current version December 15, 2015. This work was supported by the CRD, DG, and CREATE PERSWADE Programs of NSERC and a Discovery Accelerator Supplement Award from NSERC. The associate editor coordinating the review of this paper and approving it for publication was M. C. Gursoy.

The authors are with the EMT Center, INRS, Montreal, QC, H5A1K6, Canada (e-mail: zaidi@emt.inrs.ca; affes@emt.inrs.ca).

Color versions of one or more of the figures in this paper are available online at http://ieeexplore.ieee.org.

Digital Object Identifier 10.1109/TCOMM.2015.2495286

(i.e, single-ray) channels. This assumption allows terminals to avoid CSI estimation since the latter will then only depend on each terminal's location and the source and interference DoAs [12], [13]. Several monochromatic CBs (MCB)s have been proposed [12]–[18], but unfortunately shown [19]–[22] to perform poorly over polychromatic (i.e., multi-ray) channels due to mismatch. At very small values of the angular spread (AS), the latter results into slight deterioration that becomes, however, quickly unsatisfactory at moderate to large AS. In other words, any overhead gain of MCB against OCB can be achieved only at the expense of some performance loss. Furthermore, this gain is far from being sufficient since MCB's overhead remains linearly dependent on K and M_I. Some attempts have actually been made to further reduce MCB's overhead [23], [24] but only to exacerbate, despite their relevance, the already-poor MCB performance losses. To sum up, so far, only OCB and MCB solutions could be used to handle environments wherein both interference and scattering exist. The first nominally (i.e., in ideal conditions) performs optimally but incurs a huge overhead, while the second relatively reduces overhead but performs poorly. This work aims precisely to develop a new CB solution that approaches the OCB's high performance level at a very low overhead-cost.

In this paper, we consider a dual-hop communication from a source surrounded by M_I interferences to a receiver, through a wireless network comprised of K independent terminals. In the first time slot, all sources send their signals to the network while, in the second time slot, the terminals multiply the received signal by their respective beamforming weights and forward the resulting signals to the receiver. We design these weights so as to minimize the interferences plus noises' powers while maintaining the received power from the source to a constant level. We show, however, that they are intractable in closed-form due to the complexity of the polychromatic channels arising from the presence of scattering. By exploiting a two-ray channel approximation proved valid at relatively low angular spread (AS) values, we are able to derive the new optimum weights and prove that they could be locally computed at each terminal, thereby complying with the distributed feature of the network of interest. The so-obtained bichromatic distributed collaborative beamforming (B-DCB) is then analyzed and compared in performance to the monochromatic CB (MCB), whose design does not account for scattering, and the optimal CSI-based CB (OCB). Comparisons are made under both ideal and real-world conditions where we account for implementation errors and the overhead incurred by each CB solution. They reveal that the proposed B-DCB always outperforms MCB in practice; and that it approaches OCB in lightly- to moderately-scattered environments under ideal conditions and outperforms it under real-world conditions even in highly-scattered environments. We show, indeed, that the proposed B-DCB is able to approach OCB in terms of average signal-to-interference-plus-noise ratio (ASINR) in lightly- to moderately-scattered environments where AS values do not exceed 17 degrees. Consequently, it can achieve until 6 dB of ASINR gain against MCB which does not account for scattering. We further compare the three CBs in terms of ASINR achieved under real-word conditions (i.e., accounting for implementation errors). We hence prove that the proposed B-DCB outperforms OCB in lightly- to moderately-scattered environments at relatively high Doppler, thereby increasing its operational region in terms of AS values over which it is favored against the latter. Under such conditions, B-DCB always outperforms MCB in practice. Moreover, we push the comparisons to the throughput level that accounts for the overhead incurred by each solution. We show that B-DCB is able, even at high AS values, to outperform OCB which is then further penalized by its increasingly huger overhead with larger K, M_I, and/or Doppler. In such a case, indeed, the B-DCB operational region could reach until 50 degrees and, hence, cover about the entire span of AS values.

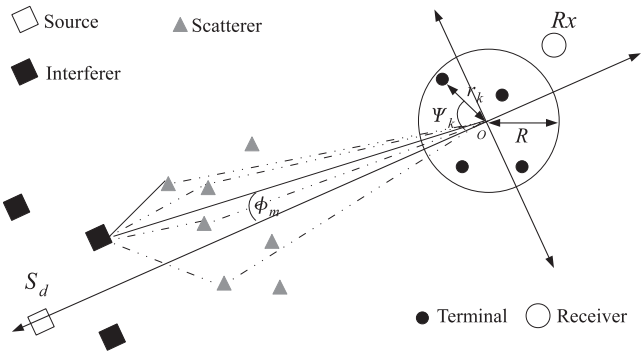

Fig. 1. System model.

Notation: Uppercase and lowercase bold letters denote matrices and vectors, respectively. $[\cdot]_{il}$ and $[\cdot]_i$ are the (i,l)-th entry of a matrix and i-th entry of a vector, respectively. $\mathbf{I}$ is the identity matrix. $(\cdot)^T$ and $(\cdot)^H$ denote the transpose and the Hermitian transpose, respectively. $\|\cdot\|$ is the 2-norm of a vector and $|\cdot|$ is the absolute value. $\mathrm{E}\{\cdot\}$ stands for the statistical expectation and $(\xrightarrow{ep1})$ $\xrightarrow{p1}$ denotes (element-wise) convergence with probability one. $J_1(\cdot)$ is the first-order Bessel function of the first kind and $\odot$ is the element-wise product.

II. System Model

As illustrated in Fig. 1, the system of interest consists of a wireless network or subnetwork comprised of K terminals equipped each with a single isotropic antenna and uniformly and independently distributed on $D(O,R)$, the disc with center at O and radius R, a receiver Rx, and M far-field sources including a desired source S_{d} and M_I interfering sources. All sources are located in the same plane[1] containing $D(O,R)$ [12], [13]. We assume that there is no direct link from the latters to the receiver due to high pathloss attenuation. Moreover, let (r_k,ψ_k) denote the polar coordinates of the k-th terminal and (A_m,ϕ_m) those of the m-th source. Without loss of generality, (A_1,ϕ_1) is assumed to be the location of S_{d} with $\phi_1=0$. Since the sources are in the far-field, we hence assume that $A_m \gg R$ for $m=1,\ldots,M$ where $M=M_I+1$.

[1]Please note that this assumption is only made for the sake of simplicity. All the results in this paper could be easily generalized to the case wherein sources are located in different planes.

The following assumptions are further adopted throughout this paper:

A1) The m-th source is scattered by a given number of scatterers located in the same plane containing $D(O, R)$. The latter generate from the transmit signal L_m rays or "spatial chromatics" (with reference to their angular distribution) that form a polychromatic propagation channel [19], [26]– [28]. The l-th ray or chromatic is characterized by its angle deviation $\theta_{l,m}$ from the m-th source direction ϕ_m and its complex amplitude $\alpha_{l,m}$. The $\theta_{l,m}$, $l = 1, \ldots, L$ are i.i.d. zero-mean random variables with a symmetric probability density function (pdf) $p_m(\theta)$ and variance σ_m^2. Note that the standard deviation σ_m is commonly known as the angular spread (AS) while $p_m(\theta)$ is called the scattering or angular distribution [26]– [28]. The $\alpha_{l,m}$ $l = 1, \ldots, L$ are i.i.d zero-mean random variables with $\mathrm{E}\left\{|\alpha_{l,m}|^2\right\} = 1/L_m$. All $\theta_{l,m}$ and $\alpha_{l,m}$ for $m = 1, \ldots, M$ and $l = 1, \ldots, L_m$ are assumed to be mutually independent.

A2) The forward channel gain $[\mathbf{f}]_k$ from the k-th terminal to the receiver is a zero-mean unit-variance circular Gaussian random variable [23], [29]– [31].

A3) The m-th source's signal s_m is narrow-band zero-mean random variable with power p_m while noises at terminals and the receiver are zero-mean Gaussian random variables with variances $\sigma_{n_t}^2$ and $\sigma_{n_r}^2$, respectively. All signals, noises, and the terminals' forward channel gains are mutually independent [5], [6], [20].

A4) The k-th terminal is only aware of its own coordinates (r_k, ψ_k), its forward channel $[\mathbf{f}]_k$, K, the wavelength λ while being oblivious to the locations and the forward channels of *all* other terminals in the network [20], [23] [24].

Resorting to A1 and the fact that $A_m \gg R$ for $m = 1, \ldots, M$, the backward channel gain from the m-th source to the k-th terminal can be represented as

$$[\mathbf{g}_m]_k = \sum_{l=1}^{L_m} \alpha_{l,m} e^{-j\frac{2\pi}{\lambda} r_k \cos(\phi_m + \theta_{l,m} - \psi_k)}. \tag{1}$$

Obviously, when the scattering effect is neglected (i.e., $\sigma_m \longrightarrow 0$) to assume a monochromatic plane-wave propagation channel, we have $\theta_{l,m} = 0$ and, hence, $[\mathbf{g}_m]_k$ could be reduced to $\left[\mathbf{g}_m^{(1)}\right]_k = e^{-j(2\pi/\lambda) r_k \cos(\phi_m - \psi_k)}$, the well-known steering vector element in the array-processing literature [12]–[24].

The communication link between the desired source S_d and the receiver is established using the following dual-hop scheme. In the first time slot, all sources send their signals to the wireless network. Let $\mathbf{y}$ denote the received signal vector at the terminals given by

$$\mathbf{y} = \mathbf{G}\mathbf{s} + \mathbf{n}_t, \tag{2}$$

where $\mathbf{s} \triangleq [s_1 s_2 \ldots s_M]^T$, $\mathbf{G} \triangleq [\mathbf{g}_1 \ldots \mathbf{g}_M]$, and $\mathbf{n}_t$ is the terminals' noise vector. In the second time slot, the k-th terminal multiplies its received signal with the complex conjugate of its beamforming weight w_k and forwards the resulting signal to the receiver Rx. The received signal r at the latter is given by

$$r = s_1 \mathbf{w}^H \mathbf{h}_1 + \mathbf{w}^H \mathbf{H}_{\bar{1}} \mathbf{s}_{\bar{1}} + \mathbf{w}^H (\mathbf{f} \odot \mathbf{n}_t) + n_r, \tag{3}$$

where n_r is the noise at Rx, $\mathbf{s}_{\bar{1}} \triangleq [s_2 \ldots s_M]^T$, $\mathbf{h}_1 \triangleq \mathbf{f} \odot \mathbf{g}_1$ and $\mathbf{H}_{\bar{1}} \triangleq [\mathbf{f} \odot \mathbf{g}_2 \ldots \mathbf{f} \odot \mathbf{g}_M]$ with $\mathbf{f} \triangleq [[\mathbf{f}]_1 \ldots [\mathbf{f}]_K]^T$. It follows from (3) that the desired power $P_{\mathbf{w},d}$ received from S_d and the undesired power $P_{\mathbf{w},u}$ from both the interference and noise are, respectively, given at the receiver by

$$P_{\mathbf{w},d} = p_1 \mathbf{w}^H \mathrm{E}\left\{\mathbf{h}_1 \mathbf{h}_1^H\right\} \mathbf{w}, \tag{4}$$

$$P_{\mathbf{w},u} = \mathbf{w}^H \mathrm{E}\left\{\mathbf{H}_{\bar{1}} \mathbf{P}_{\bar{1}} \mathbf{H}_{\bar{1}}^H\right\} \mathbf{w} + \sigma_{n_t}^2 \mathbf{w}^H \mathbf{\Sigma} \mathbf{w} + \sigma_{n_r}^2, \tag{5}$$

where $\mathbf{P}_{\bar{1}} \triangleq \mathrm{diag}\{p_2 \ldots p_M\}$, and $\Sigma \triangleq \mathrm{diag}\{|[\mathbf{f}]_1|^2 \ldots |[\mathbf{f}]_k|^2\}$. Note that the expectations in (4) and (5) are taken with respect to the rays' directions $\theta_{l,m}$s and their complex amplitudes $\alpha_{l,m}$s. Although several approaches can be adopted to properly design the beamforming weights, we are only concerned in this paper with the one which minimizes the undesired power $P_{\mathbf{w},u}$ while maintaining the desired power $P_{\mathbf{w},d}$ equal to p_1. In fact, this approach is nothing else but the well-known minimum variance distortionless response (MVDR) beamformer [32], [33] with a relaxed distortionless response constraint. The latter is imposed here on the received power from the desired source S_d (i.e., $P_{\mathbf{w},d} = p_1$) instead of the beamforming response to S_d's direction (i.e., $\mathbf{w}^H \mathbf{h}_1 = 1$). Mathematically speaking, we have to solve the following optimization problem:

$$\begin{aligned} \min_{\mathbf{w}} \; & \mathbf{w}^H \mathrm{E}\left\{\mathbf{H}_{\bar{1}} \mathbf{P}_{\bar{1}} \mathbf{H}_{\bar{1}}^H\right\} \mathbf{w} + \sigma_{n_t}^2 \mathbf{w}^H \Sigma \mathbf{w} + \sigma_{n_r}^2 \\ & \text{s.t } \mathbf{w}^H \mathrm{E}\left\{\mathbf{h}_1 \mathbf{h}_1^H\right\} \mathbf{w} = 1, \end{aligned} \tag{6}$$

or, equivalently,

$$\begin{aligned} \max_{\mathbf{w}} \; & \frac{\mathbf{w}^H \mathrm{E}\left\{\mathbf{h}_1 \mathbf{h}_1^H\right\} \mathbf{w}}{\mathbf{w}^H \left(\mathrm{E}\left\{\mathbf{H}_{\bar{1}} \mathbf{P}_{\bar{1}} \mathbf{H}_{\bar{1}}^H\right\} + \sigma_{n_t}^2 \mathbf{\Sigma}\right) \mathbf{w}} \\ & \text{s.t. } \mathbf{w}^H \mathrm{E}\left\{\mathbf{h}_1 \mathbf{h}_1^H\right\} \mathbf{w} = 1. \end{aligned} \tag{7}$$

It is straightforward to show that the optimum solution of (7) is a scaled version of the principal eigenvector of the matrix $\left(\mathrm{E}\left\{\mathbf{H}_{\bar{1}} \mathbf{P}_{\bar{1}} \mathbf{H}_{\bar{1}}^H\right\} + \sigma_{n_t}^2 \mathbf{\Sigma}\right)^{-1} \mathrm{E}\left\{\mathbf{h} h^H\right\}$ so as to satisfy the constraint in (7) [5], [20], [34]. To the best of our knowledge, this eigenvector cannot be obtained in a closed-form but could be numerically evaluated. However, besides being computationally demanding, this task must be performed by a central processor with global knowledge of all network parameters. The considered network lacks, unfortunately, such a processor.

III. Proposed CB Solution

In this section, we prove under mild conditions that it is possible to derive an optimal solution of (7) in closed-form. To this end, we exploit useful approximations of the matrices $\mathrm{E}\left\{\mathbf{h}_1 \mathbf{h}_1^H\right\}$ and $\mathrm{E}\left\{\mathbf{H}_{\bar{1}} \mathbf{P}_{\bar{1}} \mathbf{H}_{\bar{1}}^H\right\}$ that have the additional benefit of reducing by the same token the complexity of our CB

optimization problem. As such, from the assumption A1, we have

$$\mathrm{E}\left\{\mathbf{h}_m\mathbf{h}_m^H\right\} = \int_{\Theta_m} p_m(\theta)\mathbf{a}(\phi_m+\theta)\mathbf{a}^H(\phi_m+\theta)d\theta, \quad (8)$$

where $\mathbf{a}(\theta) \triangleq \left[[\mathbf{a}(\theta)]_1 \ldots [\mathbf{a}(\theta)]_K\right]^T$ with $[\mathbf{a}(\theta)]_k = [\mathbf{f}]_k e^{-j(2\pi/\lambda)r_k\cos(\theta-\psi_k)}$ and Θ_m is the support of the pdf $p_m(\theta)$ over which the integral is calculated.[2] When the AS σ_m is relatively small,[3] small angular deviations of $\theta_{l,m}$s occur and, hence, the Taylor series expansion of $\mathbf{a}(\phi_m+\theta)$ at ϕ_m yields

$$\mathbf{a}(\phi_m+\theta) \simeq \mathbf{a}(\phi_m) + \mathbf{a}'(\phi_m)\theta + \mathbf{a}''(\phi_m)\frac{\theta^2}{2}, \quad (9)$$

where $\mathbf{a}'(\theta)$ and $\mathbf{a}''(\theta)$ are, respectively, the first and the second derivatives of $\mathbf{a}(\theta)$. After substituting (9) in (8) and integrating in the latter, we have

$$\mathrm{E}\left\{\mathbf{h}_m\mathbf{h}_m^H\right\} \simeq \frac{1}{2}\Big(\mathbf{a}(\phi_m+\sigma_m)\,\mathbf{a}(\phi_m+\sigma_m)^H + \mathbf{a}(\phi_m-\sigma_m)\,\mathbf{a}(\phi_m-\sigma_m)^H\Big). \quad (10)$$

It is noteworthy that the result in (10) also holds with strict equality in the case of bichromatic (i.e., two-ray) channels (i.e., $L_m = 2$) with rays located at angles σ_m and $-\sigma_m$ where the channel gain from the m-th source to the k-th terminal is

$$\left[\mathbf{g}_m^{(2)}\right]_k = \alpha_{1,m}e^{-j\frac{2\pi}{\lambda}r_k\cos(\phi_m+\sigma_m-\psi_k)} + \alpha_{2,m}e^{-j\frac{2\pi}{\lambda}r_k\cos(\phi_m-\sigma_m-\psi_k)}. \quad (11)$$

Consequently, when the AS is typically small to moderate, the polychromatic channel $\mathbf{g}_m$ could be substituted with the bichromatic channel $\mathbf{g}_m^{(2)}$. In what follows, we will show that this bichromatic approach provides a closed-form optimal solution of (7) implementable in a distributed fashion.

It holds from (10) that

$$\mathrm{E}\left\{\mathbf{h}_1\mathbf{h}_1^H\right\} = \frac{1}{2}\boldsymbol{\Xi}, \quad (12)$$

and

$$\mathrm{E}\left\{\mathbf{H}_{\bar{1}}\mathbf{P}_{\bar{1}}\mathbf{H}_{\bar{1}}^H\right\} \approx \boldsymbol{\Gamma}\boldsymbol{\Lambda}\boldsymbol{\Gamma}^H, \quad (13)$$

where $\boldsymbol{\Xi} = \mathbf{a}(\sigma_1)\mathbf{a}(\sigma_1)^H + \mathbf{a}(-\sigma_1)\mathbf{a}(-\sigma_1)^H$, $\boldsymbol{\Gamma} = \left[\mathbf{a}(\tilde{\phi}_3), \mathbf{a}(\tilde{\phi}_4), \ldots, \mathbf{a}(\tilde{\phi}_{2M})\right]$ with $\tilde{\phi}_m = \phi_{m/2} - \sigma_{m/2}$ if m is even and $\tilde{\phi}_m = \phi_{(m-1)/2+1} + \sigma_{(m-1)/2+1}$ if m is odd, and $\boldsymbol{\Lambda} = (1/2)\left[p_2, p_2, \ldots, p_M, p_M\right]$. Therefore, when σ_m, $m = 1, \ldots, M$ are relatively small, (7) could be rewritten as

$$\max_{\mathbf{w}} \frac{\mathbf{w}^H\boldsymbol{\Xi}\mathbf{w}}{\mathbf{w}^H\left(\boldsymbol{\Gamma}\boldsymbol{\Lambda}\boldsymbol{\Gamma}^H + \sigma_{n_t}^2\Sigma\right)\mathbf{w}} \quad \text{s.t.} \quad \mathbf{w}^H\boldsymbol{\Xi}\mathbf{w} = 2, \quad (14)$$

or, equivalently as,

$$\max_{\boldsymbol{\gamma}} \frac{\boldsymbol{\gamma}^H\tilde{\boldsymbol{\Xi}}\boldsymbol{\gamma}}{\boldsymbol{\gamma}^H\boldsymbol{\gamma}} \quad \text{s.t.} \quad \boldsymbol{\gamma}^H\tilde{\boldsymbol{\Xi}}\boldsymbol{\gamma} = 2, \quad (15)$$

where $\boldsymbol{\gamma} = \boldsymbol{\Delta}^{\frac{1}{2}}\mathbf{w}$, $\boldsymbol{\Delta} = \boldsymbol{\Gamma}\boldsymbol{\Lambda}\boldsymbol{\Gamma}^H + \sigma_{n_t}^2\Sigma$, and $\tilde{\boldsymbol{\Xi}} = \boldsymbol{\Delta}^{-\frac{1}{2}}\boldsymbol{\Xi}\boldsymbol{\Delta}^{-\frac{1}{2}}$. It is straightforward to show that the optimum solution of (15) is the principal eigenvector of the matrix $\tilde{\boldsymbol{\Xi}}$ scaled to satisfy the constraint in (15). Since $\boldsymbol{\Delta}^{-\frac{1}{2}}$ is a full-rank matrix, $\tilde{\boldsymbol{\Xi}}$ has the same rank as $\boldsymbol{\Xi}$ that is inferior or equal to two. Therefore, $\tilde{\boldsymbol{\Xi}}$ has at most two eigenvectors. In the sequel, we will prove that both $\boldsymbol{\Delta}^{-\frac{1}{2}}(\mathbf{a}(\sigma_1)+\mathbf{a}(-\sigma_1))$ and $\boldsymbol{\Delta}^{-\frac{1}{2}}(\mathbf{a}(\sigma_1)-\mathbf{a}(-\sigma_1))$ are eigenvectors of $\tilde{\boldsymbol{\Xi}}$. First, let us use the matrix inversion lemma to break $\boldsymbol{\Delta}^{-1}$ into several terms and, hence, obtain

$$\tilde{\boldsymbol{\Xi}}\boldsymbol{\Delta}^{-\frac{1}{2}}(\mathbf{a}(\sigma_1)+\mathbf{a}(-\sigma_1)) = \frac{K}{\sigma_{n_t}^2} \times \Big(\boldsymbol{\Delta}^{-\frac{1}{2}}\mathbf{a}(\sigma_1)\Big(1+\chi-\boldsymbol{\chi}(\sigma_1)^H\mathbf{D}^{-1}(\boldsymbol{\chi}(\sigma_1)+\boldsymbol{\chi}(-\sigma_1))\Big) + \boldsymbol{\Delta}^{-\frac{1}{2}}\mathbf{a}(-\sigma_1)\Big(1+\chi^*-\boldsymbol{\chi}(-\sigma_1)^H\mathbf{D}^{-1}(\boldsymbol{\chi}(\sigma_1)+\boldsymbol{\chi}(-\sigma_1))\Big)\Big), \quad (16)$$

and

$$\tilde{\boldsymbol{\Xi}}\boldsymbol{\Delta}^{-\frac{1}{2}}(\mathbf{a}(\sigma_1)-\mathbf{a}(-\sigma_1)) = \frac{K}{\sigma_{n_t}^2} \times \Big(\boldsymbol{\Delta}^{-\frac{1}{2}}\mathbf{a}(\sigma_1)\Big(1-\chi-\boldsymbol{\chi}(\sigma_1)^H\mathbf{D}^{-1}(\boldsymbol{\chi}(\sigma_1)-\boldsymbol{\chi}(-\sigma_1))\Big) - \boldsymbol{\Delta}^{-\frac{1}{2}}\mathbf{a}(-\sigma_1)\Big(1-\chi^*-\boldsymbol{\chi}(-\sigma_1)^H\mathbf{D}^{-1}(\boldsymbol{\chi}(\sigma_1)-\boldsymbol{\chi}(-\sigma_1))\Big)\Big), \quad (17)$$

where $\chi = \left(\mathbf{a}^H(\sigma_1)\Sigma^{-1}\mathbf{a}(-\sigma_1)\right)/K$, $\boldsymbol{\chi}(\theta) = \left(\boldsymbol{\Gamma}^H\Sigma^{-1}\mathbf{a}(\theta)\right)/K$, and $\mathbf{D} = \left(\sigma_{n_t}^2\boldsymbol{\Lambda}^{-1} + \boldsymbol{\Gamma}^H\Sigma^{-1}\boldsymbol{\Gamma}\right)/K$. Now, we introduce the important theorem below.

Theorem 1: When K goes to infinity,[4] we have

$$\mathbf{a}(x)^H\Sigma^{-1}\mathbf{a}(y) \xrightarrow{p1} 2\frac{J_1(\gamma(x-y))}{\gamma(x-y)}, \quad (18)$$

where $\gamma(\phi) \triangleq 4\pi(R/\lambda)\sin(\phi/2)$.

Proof: It follows from the definition of $\mathbf{a}(\theta)$ that $(\mathbf{a}(x)^H\Sigma^{-1}\mathbf{a}(y))/K = (1/K)\sum_{k=1}^K e^{j\gamma(x-y)z_k}$ where z_k, $k = 1, \ldots, K$ are i.i.d compound random variables with the pdf $f_{z_k}(z) = \frac{2}{\pi}\sqrt{1-z^2}$ for $-1 \le z \le 1$. Using the strong law of large numbers and the fact that $(2/\pi)\int_{-1}^1 e^{j\gamma(\phi)z}\sqrt{1-z^2}dz = 2J_1(\gamma(\phi))/\gamma(\phi)$, we obtain (18).

It can be then inferred from this theorem that for large K

$$\chi \xrightarrow{p1} 2\frac{J_1(\gamma(2\sigma_1))}{\gamma(2\sigma_1)}, \quad (19)$$

$$\boldsymbol{\chi}(\theta) \xrightarrow{p1} 2\mathbf{z}(\theta), \quad (20)$$

$$\mathbf{D} \xrightarrow{p1} 2\mathbf{Q}, \quad (21)$$

where $\mathbf{Q}$ is a $(2M-2)\times(2M-2)$ matrix with $[\mathbf{Q}]_{mn} = J_1(\gamma(\tilde{\phi}_{m+2}-\tilde{\phi}_{n+2}))/\gamma(\tilde{\phi}_{m+2}-\tilde{\phi}_{n+2})$ if $m \neq n$ and $[\mathbf{Q}]_{mn} =$

[2] In the Gaussian and Uniform distribution cases, $\Theta_m = [-\inf, +\inf]$ and $\Theta_m = [-\sqrt{3}\sigma_{\theta m}, +\sqrt{3}\sigma_{\theta m}]$, respectively.

[3] This condition is assumed for the sole sake of mathematical rigor, without imposing any limitation on AS values in absolute terms. Simulations in Section VII will later suggest that practical AS values as high as 17 degrees still keep the following developments valid.

[4] We will actually see in Section VII that practical values of K in the range of 20 already keep the following developments valid.

$1/2$ otherwise, and $\mathbf{z}(\theta)$ is a $(2M-2)\times 1$ vector with $[\mathbf{z}(\theta)]_m = J_1(\gamma(\theta-\tilde{\phi}_{m+2}))/\gamma(\theta-\tilde{\phi}_{m+2})$ if $\theta \neq \tilde{\phi}_{m+2}$ and $[\mathbf{z}(\theta)]_m = 1/2$ otherwise. When $\sigma_m,\ m=1,\ldots,M$ are relatively small, we have $\mathbf{z}(\sigma_1) \simeq \mathbf{z}(-\sigma_1)$ and, hence, it holds from (16)–(21) that, for large K, the eigenvalues associated with $\mathbf{\Delta}^{-\frac{1}{2}}(\mathbf{a}(\sigma_1)+\mathbf{a}(-\sigma_1))$ and $\mathbf{\Delta}^{-\frac{1}{2}}(\mathbf{a}(\sigma_1)-\mathbf{a}(-\sigma_1))$ are

$$\rho_1(\sigma_1) \simeq \frac{K}{\sigma_{n_t}^2}\left(1+2\frac{J_1(\gamma(2\sigma_1))}{\gamma(2\sigma_1)}-4\mathbf{z}(\sigma_1)^T\mathbf{Q}^{-1}\mathbf{z}(\sigma_1)\right), \tag{22}$$

and

$$\rho_2(\sigma_1) \simeq \frac{K}{\sigma_{n_t}^2}\left(1-2\frac{J_1(\gamma(2\sigma_1))}{\gamma(2\sigma_1)}\right), \tag{23}$$

respectively. What remains to be done to find the principal eigenvector of $\tilde{\mathbf{\Xi}}$ is then comparing the eigenvalues ρ_1 and ρ_2. As such, we introduce the theorem below.

Theorem 2: When K goes to infinity[4], we have

$$2\mathbf{z}(0)^T\mathbf{Q}^{-1}\mathbf{z}(0) \in [0,1]. \tag{24}$$

Proof: It follows from A2 and the results in (18)–(21) that

$$2\mathbf{z}(0)^T\mathbf{Q}^{-1}\mathbf{z}(0) = \lim_{K\to\infty}\frac{1}{K}\|\mathbf{P}\mathbf{a}(0)\|^2, \tag{25}$$

where $\mathbf{P}=\mathbf{\Gamma}(\mathbf{\Gamma}^H\mathbf{\Gamma})^{-1}\mathbf{\Gamma}^H$ is the orthogonal projection matrix onto the subspace spanned by the columns of $\mathbf{\Gamma}$. $\mathbf{P}\mathbf{a}(0)$ is then the projection of $\mathbf{a}(0)$ into the latter subspace and, hence, $0 \le 2\mathbf{z}(0)^T\mathbf{Q}^{-1}\mathbf{z}(0) \le \|\mathbf{a}(0)\| = 1$. While the left-hand side (LHS) inequality holds with equality if $\mathbf{a}(0)$ is orthogonal to the column span of $\mathbf{\Gamma}$, the right-hand side (RHS) inequality holds with equality if $\mathbf{a}(0)$ is in the column span of $\mathbf{\Gamma}$. The latter event is, however, highly unlikely when K is large and, hence, $2\mathbf{z}(0)^T\mathbf{Q}^{-1}\mathbf{z}(0)$ is strictly inferior to 1.

Using Theorem 2, one can readily show that $\lim_{\sigma_1\to 0}(\rho_1-\rho_2)(\sigma_1) > 0$. Therefore, there exists a real κ such that if σ_1 is small enough we have $\sigma_1 < \kappa$ then $\rho_1(\sigma_1) > \rho_2(\sigma_1)$. Consequently, for relatively small $\sigma_m,\ m=1,\ldots,M$ and large K, $\mathbf{\Delta}^{-\frac{1}{2}}(\mathbf{a}(\sigma_1)+\mathbf{a}(-\sigma_1))$ is the principal eigenvector of $\tilde{\mathbf{\Xi}}$. Finally, scaling $\mathbf{\Delta}^{-1}(\mathbf{a}(\sigma_1)+\mathbf{a}(-\sigma_1))$ to satisfy the constraint in (14) and using (19)–(21) after breaking $\mathbf{\Delta}^{-1}$ into several terms, we show for relatively small $\sigma_m,\ m=1,\ldots,M$ and large K that the optimal solution of (14) is given by

$$\mathbf{w}_{\mathrm{BD}} = \frac{\Sigma^{-1}\left(\mathbf{a}(\sigma_1)+\mathbf{a}(-\sigma_1)-\mathbf{\Gamma}\mathbf{Q}^{-1}\boldsymbol{\nu}(\sigma_1)\right)}{K\left(1+2\frac{J_1(\gamma(2\sigma_1))}{\gamma(2\sigma_1)}-\boldsymbol{\nu}(\sigma_1)^T\mathbf{Q}^{-1}\boldsymbol{\nu}(\sigma_1)\right)}, \tag{26}$$

where $\boldsymbol{\nu}(\sigma_1)=\mathbf{z}(\sigma_1)+\mathbf{z}(-\sigma_1)$. Note that we denote this CB solution by $\mathbf{w}_{\mathrm{BD}}$ since it relies on the *bichromatic* approximation in (10) and, further, lends itself to a *distributed* implementation, as we will shortly see below. It can be observed from (26) that the k-th terminal's weight $[\mathbf{w}_{\mathrm{BD}}]_k$ depends, according to A4, on the information locally available at this node as well as $\sigma_m,\ m=1,\ldots,M$ and $\phi_m,\ m=1,\ldots,M$, which could be estimated at the sources and broadcasted to the network. Therefore, each terminal is able to autonomously compute its weight without requiring any information exchange with the other terminals in the network. This is in fact a very desired feature for any CB solution since it enables its distributed implementation and, hence, avoids any additional overhead due to such an exchange. Furthermore, from (26), $\mathbf{w}_{\mathrm{BD}}$ is independent of $p_m(\theta),\ m=1,\ldots,M$. This is also an outstanding feature which allows the proposed bichromatic distributed CB (B-DCB)'s implementation in any scattered environment regardless of its scattering distribution.

In the sequel, we compare in performance the proposed B-DCB with the two main conventional types of CB solutions disclosed so far in the literature, namely MCB and OCB (cf. Section I). But, let us first briefly explain in the next section these two CB benchmark types.

IV. MCB- and OCB-Type CB Solutions

So far, two main CB solution types exist for the optimization problem in (6). The first, MCB, simplifies the optimization by ignoring the presence of scattering and assuming instead monochromatic environments (i.e., $\sigma_m = 0,\ m=1,\ldots,M$). In such a case, indeed, $\mathrm{E}\{\mathbf{h}\mathbf{h}^H\}$ is reduced to $\mathbf{a}(0)\mathbf{a}^H(0)$. Since the principal eigenvector of $\mathbf{X}\mathbf{a}(0)\mathbf{a}^H(0)$ is simply $\mathbf{X}\mathbf{a}(0)$ for any given matrix $\mathbf{X}$, the MCB solution is given by

$$\mathbf{w}_{\mathrm{M}} = \frac{\left(\mathbf{A}_{\bar{1}}\mathbf{P}_{\bar{1}}\mathbf{A}_{\bar{1}}^H+\sigma_{n_t}^2\Sigma\right)^{-1}\mathbf{a}(0)}{\mathbf{a}^H(0)\left(\mathbf{A}_{\bar{1}}\mathbf{P}_{\bar{1}}\mathbf{A}_{\bar{1}}^H+\sigma_{n_t}^2\Sigma\right)^{-1}\mathbf{a}(0)}, \tag{27}$$

where $\mathbf{A}_{\bar{1}} \triangleq [\mathbf{a}(\phi_2)\ldots\mathbf{a}(\phi_M)]$. A straightforward inspection of (27) reveals that the k-th terminal's weight $[\mathbf{w}_{\mathrm{M}}]_k$ depends on all terminals' locations and forward channels. In contrast with the proposed B-DCB, the MCB is then a non-distributed solution whose implementation requires an information exchange among terminals, thereby resulting in an inevitable additional overhead cost.

The second conventional CB solution is the optimal CSI-based CB (OCB) which aims to optimize the objective function in (6) without violating its constraint by acting on the instantaneous desired and undesired powers. One can readily show that its beamforming vector $\mathbf{w}_{\mathrm{O}}$ is given by

$$\mathbf{w}_{\mathrm{O}} = \frac{\left(\mathbf{H}_{\bar{1}}\mathbf{P}_{\bar{1}}\mathbf{H}_{\bar{1}}^H+\sigma_{n_t}^2\Sigma\right)^{-1}\mathbf{h}_1}{\mathbf{h}_1^H\left(\mathbf{H}_{\bar{1}}\mathbf{P}_{\bar{1}}\mathbf{H}_{\bar{1}}^H+\sigma_{n_t}^2\Sigma\right)^{-1}\mathbf{h}_1}. \tag{28}$$

From (28), the OCB is implementable in the considered network if and only if each terminal is aware of all terminal's backward and forward channels. Consequently, like MCB, OCB is a non-distributed solution since it also requires an information exchange among terminals. Note from (26)–(28) that MCB and OCB have another drawback in contrast to the proposed B-DCB in that they both require accurate knowledge of $\sigma_{n_t}^2$ at each terminal.

V. Performance Analysis Under Ideal Conditions

In this section, we analyze and compare in performance the proposed B-DCB with MCB and OCB under ideal conditions (i.e., without accounting for implementation errors and the overhead cost).

A. CB Performance Metrics

Let $\xi_{\mathbf{w}}$ denote the achieved signal-to-interference-plus-noise ratio (SINR) using $\mathbf{w}$ and given by

$$\xi_{\mathbf{w}} = \frac{\left|\mathbf{w}^H \mathbf{h}_1 s_1\right|^2}{\left|\mathbf{w}^H \mathbf{H}_{\bar{1}} \mathbf{s}_{\bar{1}} + \mathbf{w}^H (\mathbf{f} \odot \mathbf{n}_t) + n_r\right|^2}. \tag{29}$$

From (29), $\xi_{\mathbf{w}}$ is an excessively complex function of the random variables n_r, $[\mathbf{n}_t]_k$, r_k, ψ_k and $[\mathbf{f}]_k$ for $k = 1, \ldots, K$ and $\alpha_{l,m}$ and $\theta_{l,m}$ $l = 1, \ldots, L_m$ for $m = 1, \ldots M$ and, hence, a random quantity of its own. Therefore, it is more practical to compare the CB solutions in terms of achieved average-signal-to-average-interference-plus-noise ratio (ASAINR) defined for any $\mathbf{w}$ as

$$\tilde{\xi}_{\mathbf{w}} = \frac{p_1 \mathrm{E}\left\{\left|\mathbf{w}^H \mathbf{h}_1\right|^2\right\}}{\mathrm{E}\left\{\mathbf{w}^H \mathbf{H}_{\bar{1}} \mathbf{P}_{\bar{1}} \mathbf{H}_{\bar{1}}^H \mathbf{w} + \sigma_{n_t}^2 \mathbf{w}^H \Sigma \mathbf{w}\right\} + \sigma_{n_r}^2}. \tag{30}$$

Despite being a more adequate performance metric, please note that the ASINR $\bar{\xi}_{\mathbf{w}} = \mathrm{E}\{\xi_{\mathbf{w}}\}$ cannot be adopted hereafter since, to the best of our knowledge, it appears to be untractable in closed-form. Yet in what follows, we will show that the achieved ASAINR and ASINR using any $\mathbf{w} \in \{\mathbf{w}_{\mathrm{BD}}, \mathbf{w}_{\mathrm{M}}, \mathbf{w}_{\mathrm{O}}\}$ coincide asymptotically when K grows large.[5] This nice feature is an additional incentive for the adoption of the ASAINR gain $\Upsilon(\mathbf{w}) = \tilde{\xi}_{\mathbf{w}}/\tilde{\xi}_{\mathbf{w}_{\mathrm{BD}}}$ as the link-level figure of merit to compare the proposed B-DCB with any benchmark $\mathbf{w}$.

1) ASAINR Gain of B-DCB vs. MCB: The theorem below establishes the B-DCB's ASAINR expression.

Theorem 3: For any given $p_m(\theta)$ and σ_m, $m = 1, \ldots, M$, $\tilde{\xi}_{\mathbf{w}_{\mathrm{BD}}}$ can be expressed as (31), shown at the bottom of page, where

$$\Psi(\phi_m) = \int_{\Theta_m} p_m(\theta) \left(\frac{J_1(\gamma(\phi_m + \theta + \sigma_1))}{\gamma(\phi_m + \theta + \sigma_1)} + \frac{J_1(\gamma(\phi_m + \theta - \sigma_1))}{\gamma(\phi_m + \theta - \sigma_1)} - \mathbf{z}(\phi_m + \theta)^T \mathbf{Q}^{-1} \boldsymbol{\nu}(\sigma_1) \right)^2 d\theta, \; m = 1, \ldots, M. \tag{32}$$

Proof: See Appendix A.

Note that the integrals in (32) can be computed numerically with any desired accuracy by using the most popular mathematical software packages such as Matlab or Mathematica, after selecting the proper scattering distributions $p_m(\theta)$, $m = 1, \ldots, M$. Moreover, when there is no scattering (i.e., $\sigma_m = 0$, $m = 1, \ldots, M$), we have $\mathbf{z}(\phi_n) = \mathbf{Q}\mathbf{e}_{2n-2}$ and, therefore,

$$\mathbf{z}(\phi_n)^T \mathbf{Q}^{-1} \boldsymbol{\nu}(\sigma_1) = \frac{J_1(\gamma(\phi_n + \sigma_1))}{\gamma(\phi_n + \sigma_1)} + \frac{J_1(\gamma(\phi_n - \sigma_1))}{\gamma(\phi_n - \sigma_1)}. \tag{33}$$

Substituting (33) in (32), we obtain in such a case $\Psi(\phi_m) = 0$ for $m = 1, \ldots, M$ and, hence, (31) boils down to

$$\tilde{\xi}_{\mathbf{w}_{\mathrm{BD}}} = \frac{p_1 \left(1 + 2\mathbf{z}(0)^T \mathbf{Q}^{-1} \mathbf{z}(0) \left(\frac{1}{K} - 1\right)\right)}{\sum_{m=2}^{M} \frac{p_m}{K} + \frac{\sigma_{n_t}^2}{K} + \sigma_{n_r}^2 \left(1 - 2\mathbf{z}(0)^T \mathbf{Q}^{-1} \mathbf{z}(0)\right)}. \tag{34}$$

As can be observed from (34), $\tilde{\xi}_{\mathbf{w}_{\mathrm{BD}}}$ is an increasing function of K that asymptotically approaches $\tilde{\xi}^{\max} = p1/\sigma_{n_r}^2$. Note that $\tilde{\xi}^{\max}$ is the maximum ASAINR ever achievable only when the desired power is kept constant to p_1 and the undesired one is reduced to its minimum level ever, i.e., $\sigma_{n_r}^2$, that is only by entirely nulling all the interferers. Simulations in Section VII will show that $\tilde{\xi}_{\mathbf{w}_{\mathrm{BD}}} \simeq \tilde{\xi}^{\max}$ when σ_m $m = 1, \ldots, M$ are relatively small to moderate in lightly- to moderately-scattered environments, respectively. This further proves the efficiency of the proposed B-DCB.

Now, let us turn our attention to the ASAINR achieved by MCB $\tilde{\xi}_{\mathbf{w}_{\mathrm{M}}}$. To the best of our knowledge, $\tilde{\xi}_{\mathbf{w}_{\mathrm{M}}}$ is intractable in closed-form hampering thereby its rigorous analytical study. Nevertheless, some interesting results could be obtained when K is large enough. As such, we introduce the theorem below.

Theorem 4: For any given $p_m(\theta)$ and σ_m, $m = 1, \ldots, M$, when K is large enough we have

$$\tilde{\xi}_{\mathbf{w}_{\mathrm{M}}} \simeq \frac{p_1 \Psi_{\mathrm{M}}(0)}{\sum_{m=2}^{M} p_m \Psi_{\mathrm{M}}(\phi_m) + \frac{\sigma_{n_r}^2}{4} \left(1 - 2\boldsymbol{\nu}_{\mathrm{M}}^T(0) \mathbf{Q}_{\mathrm{M}}^{-1} \boldsymbol{\nu}_{\mathrm{M}}(0)\right)^2}, \tag{35}$$

where

$$\Psi_{\mathrm{M}}(\phi_m) = \int_{\Theta_m} p_m(\theta) \left(\frac{J_1(\gamma(\phi_m + \theta))}{\gamma(\phi_m + \theta)} - \boldsymbol{\nu}_{\mathrm{M}}^T(\phi_m + \theta) \mathbf{Q}_{\mathrm{M}}^{-1} \boldsymbol{\nu}_{\mathrm{M}}(0) \right)^2 d\theta, \tag{36}$$

$\mathbf{Q}_{\mathrm{M}}$ is a $(M-1) \times (M-1)$ matrix with $[\mathbf{Q}_{\mathrm{M}}]_{mn} = J_1(\gamma(\phi_{m+1} - \phi_{n+1}))/\gamma(\phi_{m+1} - \phi_{n+1})$, and $\boldsymbol{\nu}_{\mathrm{M}}(\theta)$ is a $(M-1) \times 1$ vector with $[\boldsymbol{\nu}_{\mathrm{M}}(\theta)]_m = J_1(\gamma(\theta - \phi_{m+1}))/\gamma(\theta - \phi_{m+1})$.

Proof: See Appendix B.

It follows from (31) and (35) that if there is no scattering (i.e., $\sigma_m = 0$, $m = 1, \ldots, M$), we have $\Upsilon(\mathbf{w}_{\mathrm{M}}) \simeq 1$, when K is large enough. This means that, in such a case, MCB is

$$\tilde{\xi}_{\mathbf{w}_{\mathrm{BD}}} = \frac{p_1 \left(1 + (2(K-1)\Psi(0)) / \left(1 + 2\frac{J_1(\gamma(2\sigma_1))}{\gamma(2\sigma_1)} - \boldsymbol{\nu}(\sigma_1)^T \mathbf{Q}^{-1} \boldsymbol{\nu}(\sigma_1)\right)\right)}{\sum_{m=2}^{M} p_m \left(1 + (2(K-1)\Psi(\phi_m)) / \left(1 + 2\frac{J_1(\gamma(2\sigma_1))}{\gamma(2\sigma_1)} - \boldsymbol{\nu}(\sigma_1)^T \mathbf{Q}^{-1} \boldsymbol{\nu}(\sigma_1)\right)\right) + \sigma_{n_t}^2 + \frac{\sigma_{n_r}^2 K}{2} \left(1 + 2\frac{J_1(\gamma(2\sigma_1))}{\gamma(2\sigma_1)} - \boldsymbol{\nu}(\sigma_1)^T \mathbf{Q}^{-1} \boldsymbol{\nu}(\sigma_1)\right)}. \tag{31}$$

[5] We will later verify by simulations in Section VII that the ASAINR and ASINR almost coincide when K is just in the range of 20.

also able to achieve the maximum achievable ASAINR $\tilde{\xi}^{\max}$. This is expected since the monochromatic assumption made to derive $\mathbf{w}_{\mathrm{M}}$ becomes valid when $\sigma_m = 0,\ m = 1, \ldots, M$. Note that even though B-DCB and MCB achieve the same ASAINR in the absence of scattering, the former still keeps a precious practical implementation advantage over the latter by its distributed nature. Owing to this key feature, we will later prove in Section VI-B that B-DCB turns out to be much more efficient than MCB in terms of achieved throughput even when there is no scattering. Additionally, if all sources are sufficiently far apart to satisfy

$$\gamma\left(\tilde{\phi}_m - \tilde{\phi}_n\right) \gg \frac{3}{4} \quad m, n = 1, \ldots, 2M, \quad m \neq n, \tag{37}$$

then we have

$$\frac{J_1\left(\gamma\left(\tilde{\phi}_m - \tilde{\phi}_n\right)\right)}{\gamma\left(\tilde{\phi}_m - \tilde{\phi}_n\right)} = \sqrt{\frac{2}{\pi}} \frac{\cos\left(\gamma\left(\tilde{\phi}_m - \tilde{\phi}_n\right) - \frac{3\pi}{4}\right)}{\gamma\left(\tilde{\phi}_m - \tilde{\phi}_n\right)}, \tag{38}$$

and, hence, $[\boldsymbol{\nu}(\sigma_1)]_m \simeq 0,\ m = 1, \ldots, 2M$ and $[\boldsymbol{\nu}_{\mathrm{M}}(0)]_m \simeq 1,\ m = 1, \ldots, M$. Therefore, it holds that $\boldsymbol{\nu}(\sigma_1)^T \mathbf{Q}^{-1} \boldsymbol{\nu}(\sigma_1) \ll 1$ and $\boldsymbol{\nu}_{\mathrm{M}}^T(0) \mathbf{Q}_{\mathrm{M}}^{-1} \boldsymbol{\nu}_{\mathrm{M}}(0) \ll 1$. Besides, if $\sigma_m,\ m = 2, \ldots, M$ are relatively small, i.e., in lightly- to moderately-scattered environments, one could easily show that both $\Psi(\phi_m) \simeq 0$ and $\Psi_{\mathrm{M}}(\phi_m) \simeq 0,\ m = 1, \ldots, M$. Consequently, the ASAINR gain of MCB against B-DCB boils down to $\Upsilon(\mathbf{w}_{\mathrm{M}}) \simeq \Psi_{\mathrm{M}}(0)\left(1 + 2J_1(\gamma(2\sigma_1))/\gamma(2\sigma_1)\right)^2 / \Psi(0)$ for any σ_1 and large K. In particular, when σ_1 is also small, the Taylor series expansion of $J_1(\gamma(\theta \pm \sigma_1))/\gamma(\theta \pm \sigma_1)$ at θ yields

$$\frac{J_1(\gamma(\theta \pm \sigma_1))}{\gamma(\theta \pm \sigma_1)} = \frac{J_1(\gamma(\theta))}{\gamma(\theta)} \pm \sigma_1 \left(\frac{J_1(\gamma(x))}{\gamma(x)}\right)' \Bigg|_{x=\theta}, \tag{39}$$

and, hence, $\Psi(0) \simeq 4\Psi_{\mathrm{M}}(0)$. Accordingly, it holds for large K that

$$\Upsilon(\mathbf{w}_{\mathrm{M}}) \simeq \frac{1}{4}\left(1 +_0 F_1\left(;2; -4\pi^2\left(\frac{R}{\lambda}\right)^2 \sigma_1^2\right)\right)^2, \tag{40}$$

where ${}_0F_1\left(;2; -4\pi^2\left(\frac{R}{\lambda}\right)^2 x^2\right)$ is the hypergeometric function strictly decreasing at x near 0. When σ_ms are relatively small in lightly- to moderately-scattered environments, the ASAINR gain of $\mathbf{w}_{\mathrm{BD}}$ against $\mathbf{w}_{\mathrm{M}}$ derived without accounting for scattering increases with σ_1. This proves the importance of accounting for scattering when designing the proposed B-DCB. Furthermore, when σ_1 is relatively large in highly-scattered environments, we easily prove using the approximation $J_1(\gamma(x)/\gamma(x) \simeq 0$ for large x that $\Psi(0) \simeq (1/\sqrt{3}\sigma_1) \int_{-\sigma_1}^{(\sqrt{3}-1)\sigma_1} (J_1(\gamma(\theta))/\gamma(\theta))^2\, d\theta$ if $p_1(\theta)$ is Uniform. In such a case, it holds then that $\Psi(0) > \Psi_{\mathrm{M}}(0)$ and, hence, $\Upsilon(\mathbf{w}_{\mathrm{M}}) > 1$ for any large σ_1. Consequently, the proposed B-DCB always outperforms its MCB counterpart when σ_1 is relatively large in highly-scattered environments. We will later show in Section VII that this key result still holds when all $\sigma_m,\ m = 1, \ldots, M$ are relatively large as well, thereby proving even further B-DCB's efficiency.

2) ASAINR Gain of B-DCB vs. OCB: The theorem below establishes the OCB's ASAINR.

Theorem 5: For any given $p_m(\theta)$ and $\sigma_m,\ m = 1, \ldots, M$, we have

$$\tilde{\xi}_{\mathbf{w}_{\mathrm{O}}} = \frac{p_1}{\frac{\sigma_{n_t}^2}{K} + \sigma_{n_r}^2}, \tag{41}$$

when L_1 is large enough.[6]

Proof: See Appendix C.

It follows from (41) that $\tilde{\xi}_{\mathbf{w}_{\mathrm{O}}} \simeq \tilde{\xi}^{\max}$ for large K regardless of $p_m(\theta)$ and $\sigma_m,\ m = 1, \ldots, M$. Therefore, OCB is able to achieve as expected the maximum achievable ASAINR in lightly-, moderately-, and even highly-scattered environments. As discussed above, since the proposed B-DCB also achieves $\tilde{\xi}^{\max}$ when $\sigma_m,\ m = 1, \ldots, M$ are small in lightly- to moderately-scattered environments, then $\Upsilon(\mathbf{w}_{\mathrm{O}}) \simeq 1$ holds when K is large enough. However, for large σ_1 in highly-scattered environments, if (37) is satisfied, we have for large K

$$\Upsilon(\mathbf{w}_{\mathrm{O}}) \simeq \frac{1}{\Psi(0)} \geq 1. \tag{42}$$

The inequality in the RHS of (42) is due to the fact that $J_1(x)/(x) \leq 1/2$ for any real x. As can be observed from (42), OCB outperforms B-DCB when σ_1 is large in highly-scattered environments. Furthermore, the ASAINR gain of OCB against B-DCB increases with σ_1, since $\Psi(0)$ is a decreasing function of the latter. Actually, we will later show numerically in Section VII that these observations hold as well when $\sigma_m,\ m = 1, \ldots, M$ are large in highly-scattered environments. Although OCB stands out to be the most efficient CB solution under ideal conditions, we will prove in the next section that it severely deteriorates in performance under real-world conditions to become less efficient than the proposed B-DCB even in highly-scattered environments.

B. Equivalence Between ASAINR and ASINR

Since the ASINR is a more revealing metric than the ASAINR, we aim to investigate in this section the relationship between $\tilde{\xi}_{\mathbf{w}}$ and $\bar{\xi}_{\mathbf{w}}$ for $\mathbf{w} \in \{\mathbf{w}_{\mathrm{BD}}, \mathbf{w}_{\mathrm{M}}, \mathbf{w}_{\mathrm{O}}\}$ for the sake of increasing even more the high value of the results obtained so far.

As far as $\mathbf{w}_{\mathrm{BD}}$ is concerned, resorting to Theorem 1 and (19)–(21), we show for large K that

$$\left|\mathbf{w}_{\mathrm{BD}}^H \mathbf{h}_m\right|^2 \xrightarrow{p1} \left| \frac{2\sum_{l=1}^{L_m} \alpha_{l,m}\left(\boldsymbol{\nu}(\sigma_1)^T \mathbf{Q}^{-1} \mathbf{z}(\phi_m + \theta_{l,m}) - \right.}{\left(1 + 2\frac{J_1(\gamma(2\sigma_1))}{\gamma(2\sigma_1)} - \boldsymbol{\nu}(\sigma_1)^T \mathbf{Q}^{-1} \boldsymbol{\nu}(\sigma_1)\right)} \right.$$
$$\left. \frac{J_1\left(\gamma\left(\phi_m + \theta_{l,m} + \sigma_1\right)\right)}{\gamma\left(\phi_m + \theta_{l,m} + \sigma_1\right)} + \frac{J_1\left(\gamma\left(\phi_m + \theta_{l,m} - \sigma_1\right)\right)}{\gamma\left(\phi_m + \theta_{l,m} - \sigma_1\right)} \right)\Bigg|^2, \tag{43}$$

for $m = 1, \ldots, M$. Since $\lim_{K \to \infty} \mathbf{w}_{\mathrm{BD}}^H \boldsymbol{\Sigma} \mathbf{w}_{\mathrm{BD}} = 0$, it follows from (43) that for large K $\xi_{\mathbf{w}_{\mathrm{BD}}}$ converges with probability one

[6]Please note that $L_m,\ m = 1, \ldots, M$ is in essence an artifact due to channel modeling by a limited number of rays. L_m tends actually to infinity in practice.

to a ratio whose numerator and denominator are statistically independent. To derive $\bar{\xi}_{\mathbf{w}_{\mathrm{BD}}}$, one must then apply the expectation operator to the RHS of (43) which yields to the following expression:

$$\frac{4\Psi(\phi_m)}{\left(1+2\frac{J_1(\gamma(2\sigma_1))}{\gamma(2\sigma_1)}-\boldsymbol{\nu}(\sigma_1)^T\mathbf{Q}^{-1}\boldsymbol{\nu}(\sigma_1)\right)}. \tag{44}$$

Using (31) and (44), we show that

$$\bar{\xi}_{\mathbf{w}_{\mathrm{BD}}} \xrightarrow{p1} \tilde{\xi}_{\mathbf{w}_{\mathrm{BD}}}, \tag{45}$$

when K is large enough. From (45), $\bar{\xi}_{\mathbf{w}_{\mathrm{BD}}}$ and $\tilde{\xi}_{\mathbf{w}_{\mathrm{BD}}}$ have the same asymptotic behaviors thereby making the ASAINR an equally meaningful performance measure. Furthermore, following similar steps as above, one could show for large K that both $\bar{\xi}_{\mathbf{w}_{\mathrm{M}}} \xrightarrow{p1} \tilde{\xi}_{\mathbf{w}_{\mathrm{M}}}$ and $\bar{\xi}_{\mathbf{w}_{\mathrm{O}}} \xrightarrow{p1} \tilde{\xi}_{\mathbf{w}_{\mathrm{O}}}$. As such, all the results of the analytical comparisons between the three CB solutions previously established in terms of ASAINR equally hold in terms of ASINR.

VI. Performance Analysis Under Real-World Conditions

Accounting for the implementation errors and overhead incurred by each CB solution, we compare herein the proposed B-DCB with its MCB and OCB benchmarks in terms of ASAINR and throughput in Sections VI-A and VI-B, respectively.

A. ASAINR CB Comparisons

1) ASAINR Gain of B-DCB vs. MCB: From (26), the B-DCB's implementation requires that the m-th source estimates, quantizes and sends $\tilde{\phi}_{2m}$ and $\tilde{\phi}_{2m-1}$, thereby resulting in both angle estimation and quantization errors. In such a case, $[\mathbf{a}(\tilde{\phi}_m)]_k$ should be substituted by

$$\left[\hat{\mathbf{a}}\left(\tilde{\phi}_m\right)\right]_k = \left[\mathbf{a}\left(\tilde{\phi}_m\right)\right]_k e^{-j\left(\left[\mathbf{e}_{\mathrm{al}}\left(\tilde{\phi}_m\right)\right]_k+\left[\mathbf{e}_{\mathrm{aq}}\left(\tilde{\phi}_m\right)\right]_k\right)}, \tag{46}$$

where $\left[\mathbf{e}_{\mathrm{al}}(\tilde{\phi}_m)\right]_k$ and $\left[\mathbf{e}_{\mathrm{aq}}(\tilde{\phi}_m)\right]_k$ are the angle's localization and quantization errors, respectively. Assuming that these errors are relatively small and resorting to the Taylor's series expansion, one can readily prove that

$$\left[\hat{\mathbf{a}}\left(\tilde{\phi}_m\right)\right]_k \simeq \left[\mathbf{a}\left(\tilde{\phi}_m\right)\right]_k + \left[\mathbf{e}_{\mathrm{a}}\left(\tilde{\phi}_m\right)\right]_k, \tag{47}$$

where $\left[\mathbf{e}_{\mathrm{a}}(\tilde{\phi}_m)\right]_k = -j\left[\mathbf{a}(\tilde{\phi}_m)\right]_k\left(\left[\mathbf{e}_{\mathrm{al}}(\tilde{\phi}_m)\right]_k + \left[\mathbf{e}_{\mathrm{aq}}(\tilde{\phi}_m)\right]_k\right)$ with variance $\sigma^2_{e_{\mathrm{a}}} = \sigma^2_{\mathrm{al}} + \sigma^2_{\mathrm{aq}}$. Using a $(B_{\mathrm{a}}+1)$-bit uniform quantization, one can easily show that $\sigma^2_{\mathrm{aq}} = 2^{-2B_{\mathrm{s}}}\frac{\pi^2}{12}$ [35]. On the other hand, to define σ^2_{al}, we exploit the CRLB developed in [36] and, hence, $\sigma^2_{\mathrm{al}} = \frac{4\sin^2\left(\frac{\pi}{K}\right)\sigma^2_{n_t}}{NK\pi^2}$ where N is the number of samples used to estimate the angle. Using (47), Theorem 1, and the fact that $\left[\mathbf{e}_{\mathrm{al}}(\tilde{\phi}_m)\right]_k$s and $\left[\mathbf{e}_{\mathrm{aq}}(\tilde{\phi}_m)\right]_k$s are zero-mean i.i.d random variables, we obtain for large K that

$$\hat{\chi} \xrightarrow{p1} 1 + 2\frac{J_1(\gamma(2\sigma_1))}{\gamma(2\sigma_1)} + 2\sigma^2_{e_{\mathrm{a}}}, \tag{48}$$

$$\hat{\boldsymbol{\chi}}(\pm\sigma_1) \xrightarrow{p1} 2\mathbf{z}(\pm\sigma_1), \tag{49}$$

$$\hat{\mathbf{D}} \xrightarrow{p1} 2\hat{\mathbf{Q}}, \tag{50}$$

where $\hat{\chi} = \left(\left(\hat{\mathbf{a}}(\sigma_1)+\hat{\mathbf{a}}(-\sigma_1)\right)^H\Sigma^{-1}\hat{\mathbf{a}}(\sigma_1)\right)/K$, $\hat{\mathbf{Q}} = \mathbf{Q} + \frac{\sigma^2_{e_{\mathrm{a}}}}{2}\mathbf{I}_{2M-2}$, $\hat{\boldsymbol{\chi}}(\theta) = \left(\hat{\boldsymbol{\Gamma}}^H\Sigma^{-1}\hat{\mathbf{a}}(\theta)\right)/K$, and $\hat{\mathbf{D}} = (\boldsymbol{\Lambda}^{-1} + \hat{\boldsymbol{\Gamma}}^H\Sigma^{-1}\hat{\boldsymbol{\Gamma}})/K$ with $\hat{\boldsymbol{\Gamma}} = \left[\hat{\mathbf{a}}(\tilde{\phi}_3), \hat{\mathbf{a}}(\tilde{\phi}_4), \ldots, \hat{\mathbf{a}}(\tilde{\phi}_{2M-1}), \hat{\mathbf{a}}(\tilde{\phi}_{2M})\right]$. It follows then from (48)–(50) that the proposed B-DCB is given under real-word conditions by

$$\hat{\mathbf{w}}_{\mathrm{BD}} = \frac{\Sigma^{-1}\left(\hat{\mathbf{a}}(\sigma_1)+\hat{\mathbf{a}}(-\sigma_1)-\hat{\boldsymbol{\Gamma}}\hat{\mathbf{E}}^{-1}\boldsymbol{\nu}(\sigma_1)\right)}{K\left(1+2\frac{J_1(\gamma(2\sigma_1))}{\gamma(2\sigma_1)}+2\sigma^2_{e_{\mathrm{a}}}-\boldsymbol{\nu}(\sigma_1)^T\hat{\mathbf{E}}^{-1}\boldsymbol{\nu}(\sigma_1)\right)}. \tag{51}$$

Using the fact that $\hat{\mathbf{Q}}^{-1} \simeq \mathbf{Q}^{-1} - (\sigma^2_{e_{\mathrm{a}}}/2)\mathbf{Q}^{-2}$ for small $\sigma^2_{e_{\mathrm{a}}}$ and following the derivation steps similar to those in Appendix A, we prove that the achieved ASIANR using $\hat{\mathbf{w}}_{\mathrm{BD}}$ is given as (52), shown at the bottom of the page. As can be observed from (52) and (31), $\tilde{\xi}_{\hat{\mathbf{w}}_{\mathrm{BD}}}$ is reduced to $\tilde{\xi}_{\mathbf{w}_{\mathrm{BD}}}$, when $\sigma^2_{e_{\mathrm{a}}} = 0$. This is expected since, in such a case, $\mathbf{w}_{\mathrm{BD}} = \hat{\mathbf{w}}_{\mathrm{BD}}$. Furthermore, from (52), if the condition in (37) is satisfied, we have for small σ_m, $m = 2\ldots M$ that

$$\tilde{\xi}_{\hat{\mathbf{w}}_{\mathrm{BD}}} = \frac{p1\left(1+2(K-1)\Psi(0)/\left(1+2\frac{J_1(\gamma(2\sigma_1))}{\gamma(2\sigma_1)}+2\sigma^2_{e_{\mathrm{a}}}\right)\right)}{\sum_{m=2}^{M}p_m+\sigma^2_{n_t}+\frac{K\sigma^2_{n_r}}{2}\left(1+2\frac{J_1(\gamma(2\sigma_1))}{\gamma(2\sigma_1)}+2\sigma^2_{e_{\mathrm{a}}}\right)}. \tag{53}$$

It follows from (53) that the ASAINR achieved by the proposed B-DCB under real-world conditions decreases with $\sigma^2_{e_{\mathrm{a}}}$, as expected.

$$\tilde{\xi}_{\hat{\mathbf{w}}_{\mathrm{BD}}} = \frac{p_1\left(1+\frac{\left(2\sigma^2_{e_{\mathrm{a}}}\boldsymbol{\nu}(\sigma_1)^T\hat{\mathbf{Q}}^{-1}\boldsymbol{\nu}(\sigma_1)+2(K-1)\left(\Psi(0)+\sigma^2_{\tilde{\mathbf{e}}}\hat{\Psi}(0)\right)\right)}{1+2\frac{J_1(\gamma(2\sigma_1))}{\gamma(2\sigma_1)}+2\sigma^2_{e_{\mathrm{a}}}-\boldsymbol{\nu}(\sigma_1)^T\hat{\mathbf{Q}}^{-1}\boldsymbol{\nu}(\sigma_1)}\right)}{\sum_{m=2}^{M}p_m\left(1+\frac{2\sigma^2_{e_{\mathrm{a}}}\boldsymbol{\nu}(\sigma_1)^T\hat{\mathbf{Q}}^{-1}\boldsymbol{\nu}(\sigma_1)+2(K-1)\left(\Psi(\phi_m)+\sigma^2_{\tilde{\mathbf{e}}}\hat{\Psi}(\phi_m)\right)}{1+2\frac{J_1(\gamma(2\sigma_1))}{\gamma(2\sigma_1)}+2\sigma^2_{e_{\mathrm{a}}}-\boldsymbol{\nu}(\sigma_1)^T\hat{\mathbf{Q}}^{-1}\boldsymbol{\nu}(\sigma_1)}\right)+\sigma^2_{n_t}+\frac{K\sigma^2_{n_r}}{2}\left(1+2\frac{J_1(\gamma(2\sigma_1))}{\gamma(2\sigma_1)}+2\sigma^2_{e_{\mathrm{a}}}-\boldsymbol{\nu}(\sigma_1)^T\hat{\mathbf{Q}}^{-1}\boldsymbol{\nu}(\sigma_1)\right)},$$

where $\hat{\Psi}(\phi_m) = \int_{\Theta_m} p_m(\theta)\mathbf{z}(\phi_m+\theta)^T\mathbf{Q}^{-2}\boldsymbol{\nu}(\sigma_1)\left(\frac{J_1(\gamma(\phi_m+\theta+\sigma_1))}{\gamma(\phi_m+\theta+\sigma_1)}+\frac{J_1(\gamma(\phi_m+\theta-\sigma_1))}{\gamma(\phi_m+\theta-\sigma_1)}-\mathbf{z}(\phi_m+\theta)^T\mathbf{Q}^{-1}\boldsymbol{\nu}(\sigma_1)\right)d\theta$. (52)

As far as MCB's implementation is concerned, (27) implies that the m-th source must only estimate, quantize, and send its direction ϕ_m. This process unfortunately results in both angle's estimation and quantization errors and, hence, the MCB solution becomes

$$\hat{\mathbf{w}}_{\mathrm{M}} = \frac{\left(\hat{\mathbf{A}}_{\bar{\mathrm{I}}}\mathbf{P}_{\bar{\mathrm{I}}}\hat{\mathbf{A}}_{\bar{\mathrm{I}}}^{H} + \Sigma\right)^{-1}\hat{\mathbf{a}}(0)}{\hat{\mathbf{a}}^{H}(0)\left(\hat{\mathbf{A}}_{\bar{\mathrm{I}}}\mathbf{P}_{\bar{\mathrm{I}}}\hat{\mathbf{A}}_{\bar{\mathrm{I}}}^{H} + \Sigma\right)^{-1}\hat{\mathbf{a}}(0)}, \tag{54}$$

where $\hat{\mathbf{A}}_{\bar{\mathrm{I}}} \triangleq \left[\hat{\mathbf{a}}(\phi_2)\ldots\hat{\mathbf{a}}(\phi_M)\right]$. Using (53) and following the same approach as in Appendix B to derive $\tilde{\xi}_{\hat{\mathbf{w}}_{\mathrm{M}}}$, we show if the condition in (37) is satisfied that

$$\hat{\Upsilon}\left(\hat{\mathbf{w}}_{\mathrm{M}}\right) \simeq \frac{\Psi_{\mathrm{M}}(0)\left(1 + 2\frac{J_1(\gamma(2\sigma_1))}{\gamma(2\sigma_1)} + 2\sigma_{e_{\mathrm{a}}}^2\right)^2}{\Psi(0)\left(1+\sigma_{e_{\mathrm{a}}}^2\right)^2}, \tag{55}$$

holds for large K and small σ_m, $m = 2,\ldots,M$. In (55), $\hat{\Upsilon}(\mathbf{w}) = \tilde{\xi}_{\mathbf{w}}/\tilde{\xi}_{\hat{\mathbf{w}}_{\mathrm{BD}}}$ and, hence, $\hat{\Upsilon}\left(\hat{\mathbf{w}}_{\mathrm{M}}\right) \simeq 1$ when there is no scattering. This is expected since both B-DCB and MCB's implementations require M quantized angle estimates and, therefore, equally suffer from their estimation and quantization errors. Besides, since $1 + 2J_1(\gamma(2\sigma_1))/\gamma(2\sigma_1) \leq 2$, $\hat{\Upsilon}\left(\hat{\mathbf{w}}_{\mathrm{M}}\right)$ is an increasing function of $\sigma_{e_{\mathrm{a}}}^2$. This implies that $\hat{\Upsilon}\left(\hat{\mathbf{w}}_{\mathrm{M}}\right) > \Upsilon(\mathbf{w}_{\mathrm{M}})$ for any $\sigma_{e_{\mathrm{a}}}^2 \neq 0$. Therefore, the ASAINR gain of B-DCB against MCB decreases under real-world conditions. This is expected since the B-DCB's implementation requires more angular information than MCB and, hence, is more affected by their estimation and quantization errors. Furthermore, from (55), the ASAINR gain of B-DCB gainst MCB may turn into losses under exceptional circumstances hard to justify in practice (e.g., low quantization level or very small B_{a} which results in large quantization errors and, consequently, in a large $\sigma_{e_{\mathrm{a}}}^2$).

2) ASAINR Gain of B-DCB vs. OCB: From (28), the OCB's implementation requires that the m-th source estimates and quantizes the channels $[\mathbf{g}_m]_k, k = 1\ldots K$ before sending them back to all K terminals, thereby resulting in both estimation and quantization errors. Let us denote the resulting channel between the m-th source and the k-th terminal by $[\hat{\mathbf{g}}_m]_k = [\mathbf{g}_m]_k + [\mathbf{e}_{\mathrm{c,m}}]_k$ where $\mathbf{e}_{\mathrm{c,m}} = \mathbf{e}_{\mathrm{ci,m}} + \mathbf{e}_{\mathrm{cq,m}}$ and $\mathbf{e}_{\mathrm{ci,m}}$ and $\mathbf{e}_{\mathrm{cq,m}}$ are the channel identification and quantization errors, respectively. Let $\sigma_{e_{\mathrm{c}}}^2 = \sigma_{\mathrm{ci}}^2 + \sigma_{\mathrm{cq}}^2$ be the variance of $[\mathbf{e}_{\mathrm{c,m}}]_k$ where σ_{ci}^2 and σ_{cq}^2 are those of $[\mathbf{e}_{\mathrm{ci,m}}]_k$ and $[\mathbf{e}_{\mathrm{cq,m}}]_k$, respectively. Assuming a $(B_{\mathrm{c}}+1)$-bit uniform quantization,[7] we have $\sigma_{\mathrm{cq}}^2 = 2^{-2B_{\mathrm{c}}}\frac{g_{\mathrm{Max}}^2}{12}$ where g_{Max} is the peak amplitude of all channels' realizations $\left[\mathbf{g}_m\right]_k$ for $k = 1,\ldots,K$ [35]. Based on [37], we have $\sigma_{\mathrm{ci}}^2 = \frac{3}{2}\left(\pi\sigma_{n_t}^2\bar{f}_{\mathrm{D}}\right)^{\frac{2}{3}}$ where $\bar{f}_{\mathrm{D}}$ is the normalized Doppler frequency. Substituting $\mathbf{h}_m$ by $\hat{\mathbf{h}}_m = \mathbf{f}\odot\hat{\mathbf{g}}_m$ in (28), we obtain the OCB's beamforming vector $\hat{\mathbf{w}}_{\mathrm{O}}$. Using the fact that $[\mathbf{e}_{\mathrm{c,m}}]_k$s are i.i.d random variables independent from the channels $[\mathbf{g}_m]_k$s and following the same derivations steps as in Appendix C, we prove that

$$\tilde{\xi}_{\hat{\mathbf{w}}_{\mathrm{O}}} \simeq \frac{p_1}{\left(1+\sigma_{e_{\mathrm{c}}}^2\right)\sigma_{n_r}^2}, \tag{56}$$

when K and L_m, $m = 2,\ldots,M$ are large enough. It can be inferred from (52) and (56) that the ASAINR gain $\hat{\Upsilon}\left(\hat{\mathbf{w}}_{\mathrm{O}}\right)$ achieved by OCB against the proposed B-DCB decreases when $\bar{f}_{\mathrm{D}}$ increases (i.e., $\sigma_{e_{\mathrm{c}}}^2$ increases). Therefore, from (52) and (56), if $\sigma_{e_{\mathrm{a}}}^2$ is sufficiently small, $\hat{\Upsilon}\left(\hat{\mathbf{w}}_{\mathrm{O}}\right) < 1$ holds in lightly- to moderately-scattered environments. In such environments, the proposed B-DCB is then able to outperform OCB. Simulations in Section VII will later show that this gain translates into a larger operational region in terms of AS values over which B-DCB is favored against OCB. Furthermore, when $\bar{f}_{\mathrm{D}}$ is large enough to satisfy

$$\bar{f}_{\mathrm{D}} > \frac{\left(\frac{2}{3}\left(\left(\sigma_{n_r}^2\tilde{\xi}_{\hat{\mathbf{w}}_{\mathrm{BD}}}\right)^{-1} - 1\right) - \sigma_{\mathrm{cq}}^2\right)^{\frac{3}{2}}}{\pi\sigma_{n_t}^2}, \tag{57}$$

then we have from (52) and (56) that $\hat{\Upsilon}\left(\hat{\mathbf{w}}_{\mathrm{O}}\right) < 1$ holds for any $p_m(\theta)$ and $\sigma_m, m = 1,\ldots,M$. Consequently, under real-world conditions and even in highly-scattered environments, the proposed B-DCB is able to outperform OCB whose performance severely deteriorates at high Doppler. This further proves once again the efficiency of the proposed CB solution.

For the sake of simplicity in the above comparisons, we have restricted the implementation errors incurred by each CB solution to the extrinsic parameters from the network perspective (i.e., ϕ_m, $\tilde{\phi}_m$, and $\mathbf{g}_m$). Indeed, we have assumed that the intrinsic parameters such as $[\mathbf{f}]_k$ and (r_k, ψ_k) are perfectly known at the k-th terminal. This simplification actually favors both MCB and OCB at the expense of the proposed B-DCB which is oblivious to the intrinsic parameters due to its distributed nature and, hence, the least affected by their estimation and quantization errors. In fact, from the discussions made in Sections III and IV, $[\mathbf{w}_{\mathrm{BD}}]_k$ is corrupted by the estimation errors of $[\mathbf{f}]_k$ and (r_k, ψ_k), like $[\mathbf{w}_{\mathrm{M}}]_k$ and $[\mathbf{w}_{\mathrm{O}}]_k$, which are, however, additionally corrupted by estimation and quantization errors of all $[\mathbf{f}]_k'$ and (r_k', ψ_k'), $k' = 1,\ldots,K$, $k' \neq k$. If such errors were accounted for, the ASAINR advantage of the proposed B-DCB over both MCB and OCB would have been far greater.

B. Link-Level Throughput CB Comparisons

The ASAINR comparisons above, despite their valuable insights, face a major weakness in that they do not factor in the different overhead costs incurred by each CB solution. Hence, comparisons in terms of the link-level throughput become crucial. Assuming without loss of generality BPSK-modulated transmissions using a Gaussian codebook, the link-level throughput achieved by $\mathbf{w}$ is given by [38]

$$\mathcal{T}_{\mathbf{w}} = 0.5\left(R_{\mathrm{T}} - R_{\mathbf{w}}^{\mathrm{oh}}\right)\mathrm{E}\left\{\log_2\left(1+\xi_{\mathbf{w}}\right)\right\}, \tag{58}$$

where R_{T} and $R_{\mathbf{w}}^{\mathrm{oh}}$ are the transmission bit rate and the overhead bit rate allocated to $\mathbf{w}$'s implementation. Obviously, $\mathcal{T}_{\mathbf{w}}$

[7]For both the sake of simplicity and tractability, we resort here to the Uniform quantization of channel estimates which is far from optimal in contrast for instance to the Grassmannian quantization scheme in [25].

is intractable in closed-form, thereby hampering its analytical study. However, exploiting the fact that $\log_2(X)$ is a concave function, the Jensen's inequality, and the results in Section V-B, we show that $\mathcal{T}_{\mathbf{w}}$ is upper bounded by

$$\tilde{\mathcal{T}}_{\mathbf{w}} = 0.5\left(R_{\mathrm{T}} - R_{\mathbf{w}}^{\mathrm{oh}}\right)\log_2\left(1+\tilde{\xi}_{\mathbf{w}}\right), \tag{59}$$

when K is large enough. In what follows, we propose, for the sake of analytical tractability, to use (59) as an alternative to (58) when comparing the proposed B-DCB with its benchmarks. The throughput gain achieved by any given beamformer $\mathbf{w}$ over the proposed B-DCB solution is therefore given by

$$\tilde{\mathcal{G}}(\mathbf{w}) = \frac{\tilde{\mathcal{T}}_{\mathbf{w}} - \tilde{\mathcal{T}}_{\mathbf{w}_{\mathrm{BD}}}}{\tilde{\mathcal{T}}_{\mathbf{w}_{\mathrm{BD}}}}. \tag{60}$$

We will shortly see below, both by analysis and simulations, that this performance metric, despite the simplifying assumptions above, is still able to provide a comparative framework that is extremely insightful qualitatively.

1) Throughput Gain of B-DCB vs. OCB: As discussed in Section IV, the proposed B-DCB implementation requires that the m-th source broadcasts $\tilde{\phi}_{2m}$ and $\tilde{\phi}_{2m-1}$. Each angle's broadcast requires one time slot of B_{a} bits transmitted at a localization refreshment rate $f_{\mathrm{LR}} = 1/T_{\mathrm{LR}}$ where T_{LR} is the refreshment period. Since the latter is typically very large, we assume that $f_{\mathrm{LR}} \simeq 0$ and, hence, we have $R_{\mathbf{w}_{\mathrm{BD}}}^{\mathrm{oh}} \simeq 0$. The throughput achieved by the proposed B-DCB is then given by

$$\tilde{\mathcal{T}}_{\hat{\mathbf{w}}_{\mathrm{BD}}} \simeq 0.5 R_{\mathrm{T}} \log_2\left(1+\tilde{\xi}_{\hat{\mathbf{w}}_{\mathrm{BD}}}\right). \tag{61}$$

On the other hand, the OCB's implementation requires that the m-th source broadcasts all $[\mathbf{g}_m]_k, k = 1 \ldots K$ for all K terminals. This process requires K time slots of B_{c} bits transmitted at an identification refreshment rate $f_{\mathrm{IR}} = 1/T_{\mathrm{IR}}$ where T_{IR} denotes the refreshment period. It is noteworthy that T_{IR} should satisfy $T_{\mathrm{IR}} \geq T_{\mathrm{c}}$ where $T_{\mathrm{c}} = 0.423/f_{\mathrm{D}}$ is the coherence time and f_{D} is the maximum Doppler frequency. For simplicity, we assume $f_{\mathrm{IR}} = 2f_{\mathrm{D}}$. The overhead rate of such process is then $2KMB_{\mathrm{c}}f_{\mathrm{D}}$. Furthermore, from (28), the OCB's implementation requires also that the k-th terminal broadcasts $[\mathbf{f}]_k$ in the network. This is in contrast to the proposed B-DCB whose implementation avoids such information exchange among terminals, thanks to its distributed nature. Assuming that B_{c} bits are allocated to $[\mathbf{f}]_k$ and refreshed every T_{IR}, the OCB's implementation overhead rate is then $R_{\hat{\mathbf{w}}_{\mathrm{O}}}^{\mathrm{oh}} = 2K(M+1)B_{\mathrm{c}}f_{\mathrm{D}}$ and, hence, its achieved throughput is

$$\tilde{\mathcal{T}}_{\hat{\mathbf{w}}_{\mathrm{O}}} = 0.5R_{\mathrm{T}}\left(1-2K(M_I+2)B_{\mathrm{c}}\bar{f}_{\mathrm{D}}\right)\log_2\left(1+\tilde{\xi}_{\hat{\mathbf{w}}_{\mathrm{O}}}\right). \tag{62}$$

As can be observed from (62), the throughput achieved by OCB decreases with the number of terminals K as well as the number of interfering sources M_I. Furthermore, since $\tilde{\xi}_{\hat{\mathbf{w}}_{\mathrm{O}}}$ decreases when $\bar{f}_{\mathrm{D}}$ increases, it follows then from the above result that $\tilde{\mathcal{T}}_{\hat{\mathbf{w}}_{\mathrm{O}}}$ also decreases if $\bar{f}_{\mathrm{D}}$ increases. Interestingly, from (62), B_{c} has two contradictory effects on $\tilde{\mathcal{T}}_{\hat{\mathbf{w}}_{\mathrm{O}}}$. Indeed, if B_{c} increases, the OCB overhead rate increases and, hence, $\tilde{\mathcal{T}}_{\hat{\mathbf{w}}_{\mathrm{O}}}$ decreases. However, from (56), increasing B_{c} (i.e., decreasing $\sigma_{e_{\mathrm{c}}}^2$) improves $\tilde{\xi}_{\hat{\mathbf{w}}_{\mathrm{O}}}$ and, therefore, the achieved throughput $\tilde{\mathcal{T}}_{\hat{\mathbf{w}}_{\mathrm{O}}}$. The result in (62) could then be exploited to find the optimum number of quantization bits $B_{\mathrm{c}}^{\mathrm{opt}}$ that maximizes the OCB's throughput. Moreover, since B-DCB's throughput is, in contrast to OCB, independent of K, M_I, and $\bar{f}_{\mathrm{D}}$, from (62) and (61), then $\tilde{\mathcal{G}}\left(\hat{\mathbf{w}}_{\mathrm{O}}\right)$ decreases if one of these parameters increases. Furthermore, if (57) is satisfied, we easily show that $\tilde{\mathcal{G}}\left(\hat{\mathbf{w}}_{\mathrm{O}}\right) < 0$. Simulations in Section VII will later show that this result translates into a wider operational region in terms of AS values over which B-DCB is favored against OCB, reaching actually as much as 50 degrees thereby covering about the entire span of AS values.

2) Throughput Gain of B-DCB vs. MCB: From (27), in order to properly implement MCB, the m-th source must only broadcast its direction ϕ_m to the network and, additionally, terminals must exchange their positions as well as their forward channels. This is in contrast to the proposed B-DCB whose implementation avoids such an exchange due to its distributed nature. Assuming that each position should be refreshed every T_{LR}, which is typically large, it can be readily shown that MCB's implementation overhead rate is $R_{\mathbf{w}_{\mathrm{M}}}^{\mathrm{oh}} = 2Kf_{\mathrm{D}}$ and, therefore,

$$\tilde{\mathcal{T}}_{\hat{\mathbf{w}}_{\mathrm{M}}} \simeq 0.5R_{\mathrm{T}}\left(1-2K\bar{f}_{\mathrm{D}}\right)\log_2\left(1+\tilde{\xi}_{\hat{\mathbf{w}}_{\mathrm{M}}}\right). \tag{63}$$

As can be observed from (63), in contrast to the proposed B-DCB, the throughput achieved by MCB decreases when K and/or $\bar{f}_{\mathrm{D}}$ increase/s. Since $\tilde{\xi}_{\hat{\mathbf{w}}_{\mathrm{M}}} \leq \tilde{\xi}_{\hat{\mathbf{w}}_{\mathrm{BD}}}$ for any p_m and $\sigma_m, m = 1, \ldots, M$ for practical values of B_{a}, then $\tilde{\mathcal{G}}\left(\hat{\mathbf{w}}_{\mathrm{M}}\right) \leq 0$ holds. From (61) and (63), this gain decreases with K and f_{D}. Consequently, under real-world conditions, the proposed B-DCB always outperforms MCB in terms of throughput. This also holds true in scattering-free environments (i.e., $\sigma_m = 0$ for $m = 1, \ldots, M$) where MCB and B-DCB achieves the same ASAINR, as proved in Section V-A1.

VII. Simulation Results

Computer simulations are provided to support the theoretical results. All empirical average quantities are calculated over 10^6 random realizations of r_k, ψ_k, $[\mathbf{f}]_k$ for $k = 1, \ldots, K$ and $\alpha_{l,m}, \theta_{l,m}$ for $l = 1, \ldots, L_m$. In all simulations, all sources have the same power $p = 1$ and $\sigma_{n_r}^2 = \sigma_{n_t}^2 = 1$. The number of rays is $L_m = 6$, $\sigma_m = \sigma$ and the scattering distribution $p_m(\theta)$ is Uniform for $m = 1, \ldots, M$, except in Fig. 2(b) where we consider a Gaussian distribution. Unless otherwise stated, $K = 20$ and $M_I = 3$ with $[\phi_2, \phi_3, \phi_4] = [10, 15, 20]$ degrees.

Fig. 2 plots, under ideal conditions, the ASAINRs $\tilde{\xi}_{\mathbf{w}_{\mathrm{BD}}}$, $\tilde{\xi}_{\mathbf{w}_{\mathrm{M}}}$, and $\tilde{\xi}_{\mathbf{w}_{\mathrm{O}}}$ and the ASINRs $\bar{\xi}_{\mathbf{w}_{\mathrm{BD}}}$, $\bar{\xi}_{\mathbf{w}_{\mathrm{M}}}$, and $\bar{\xi}_{\mathbf{w}_{\mathrm{O}}}$ versus σ. The scattering distributions $p_m(\theta), m = 1, \ldots, M$ are assumed to be Uniform in Fig. 2(a) and Gaussian in Fig. 2(b). From these figures, we confirm that the analytical $\tilde{\xi}_{\mathbf{w}_{\mathrm{BD}}}$ and $\tilde{\xi}_{\mathbf{w}_{\mathrm{O}}}$ match perfectly their empirical counterparts while (35) closely approaches the empirical $\tilde{\xi}_{\mathbf{w}_{\mathrm{BD}}}$ for $K = 20$. Both figures show that, under ideal conditions, OCB is able to reach the maximum achievable ASAINR $\tilde{\xi}^{\max}$, regardless of σ. This is due to the optimality of such a CB solution. Figs. 2(a) and 2(b) also show that the ASAINR $\tilde{\xi}_{\mathbf{w}_{\mathrm{BD}}}$ achieved by the proposed B-DCB approaches $\tilde{\xi}_{\max}$ in lightly to moderately-scattered

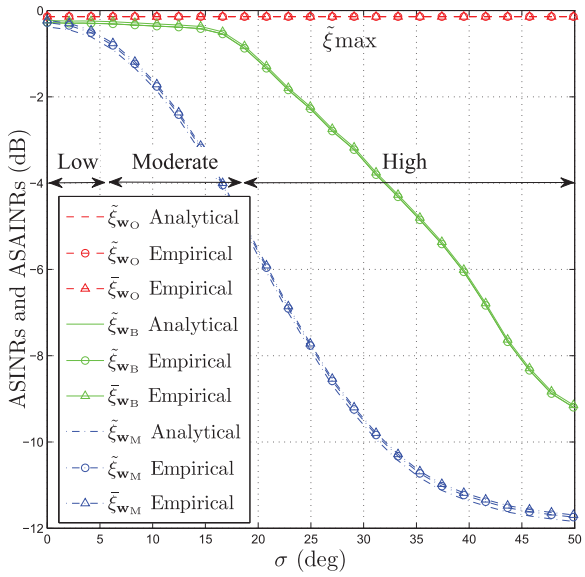

(a) Uniform distributions.

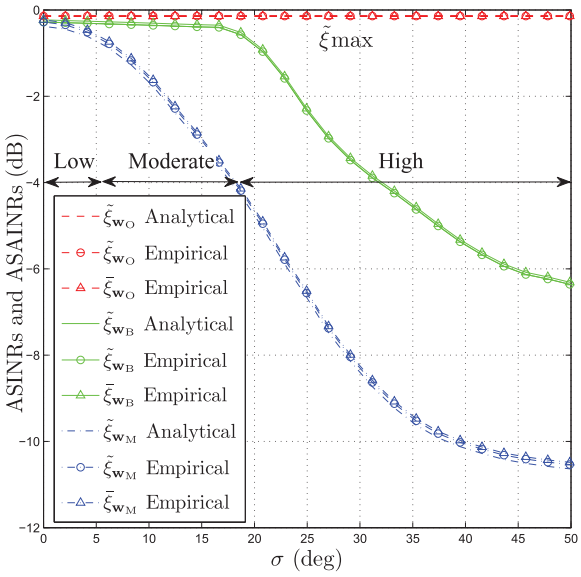

(b) Gaussian distributions.

Fig. 2. The analytical and the empirical ASAINRs achieved, under ideal conditions, by MCB, OCB, and the proposed B-DCB as well as their empirical ASINRs versus σ for $K = 20$ when the scattering distributions are (a): Uniform and (b): Gaussian.

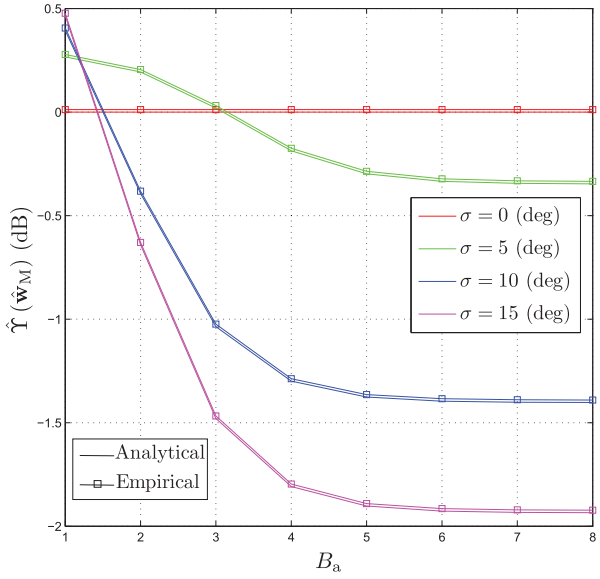

(a) $\hat{\Upsilon}(\mathbf{w}_{\mathrm{M}})$ vs. B_{a}.

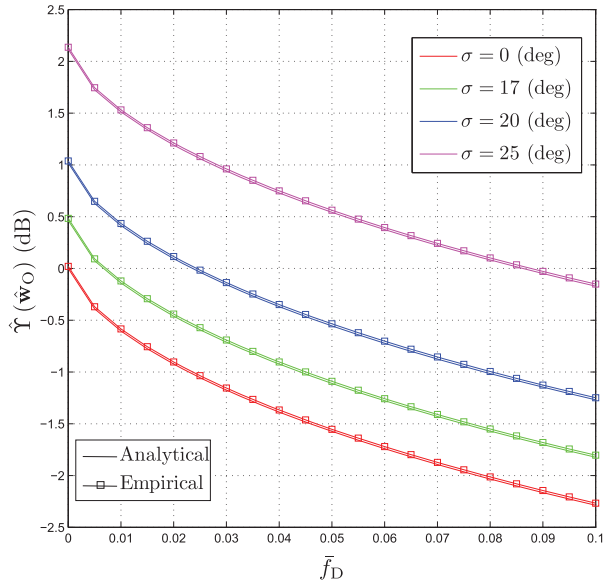

(b) $\hat{\Upsilon}(\mathbf{w}_{\mathrm{O}})$ vs. $\bar{f}_{\mathrm{D}}$.

Fig. 3. The analytical and the empirical ASAINR gains achieved, under real-world conditions, by MCB and OCB against the proposed B-DCB vs. (a): B_{a} and (b): $\bar{f}_{\mathrm{D}}$ for $K = 20$ and different values of σ.

environments where σ is in the range of 17 degrees. When the scattering distributions are Uniform, this means that the angle deviations $\theta_{l,m}$s vary from approximately -30 to 30 degrees (i.e., an angular interval of almost 60 degrees). Consequently, in lightly to moderately-scattered environments, the proposed B-DCB is also optimal. However, the ASAINR $\tilde{\xi}_{\mathbf{w}_{\mathrm{BD}}}$ achieved by B-DCB severely deteriorates in highly-scattered environments where $\sigma > 20$ degrees. Furthermore, we see from Figs. 2(a) and 2(b) that the ASAINR performed by MCB, which is designed without accounting for scattering, slightly decreases in lightly-scattered environments where σ is around 5 degrees, and becomes soon unsatisfactory in moderately- to highly-scattered environments. In such settings, the proposed B-DCB is able to achieve until 6 dB of ASAINR gain against MCB. All these observations corroborate the analytical results of Section V-A1. Moreover, from these figures, the curves of $\tilde{\xi}_{\mathbf{w}_{\mathrm{O}}}$, $\tilde{\xi}_{\mathbf{w}_{\mathrm{BD}}}$, and $\tilde{\xi}_{\mathbf{w}_{\mathrm{M}}}$ are almost indistinguishable from $\bar{\xi}_{\mathbf{w}_{\mathrm{O}}}$, $\bar{\xi}_{\mathbf{w}_{\mathrm{BD}}}$, and $\bar{\xi}_{\mathbf{w}_{\mathrm{M}}}$, respectively, when $K = 20$. Indeed, as claimed in Section V-B, the achieved ASAINRs and ASINRs become equivalent when K is large.

Fig. 3 displays the analytical and the empirical ASAINR gains achieved by $\hat{\mathbf{w}}_{\mathrm{M}}$ and $\hat{\mathbf{w}}_{\mathrm{O}}$ against $\hat{\mathbf{w}}_{\mathrm{BD}}$ for different values of σ. Fig. 3(a) plots $\hat{\Upsilon}(\hat{\mathbf{w}}_{\mathrm{M}})$ versus B_{a} for $\sigma \in \{0, 5, 10, 15\}$ degrees while Fig. 3(b) plots $\hat{\Upsilon}(\hat{\mathbf{w}}_{\mathrm{O}})$ versus $\bar{f}_{\mathrm{D}}$ for $\sigma \in \{0, 17, 20, 25\}$ degrees when $B_{\mathrm{a}} = B_{\mathrm{c}} = 8$ bits. From both figures, the analytical results of Section VI-A closely approach

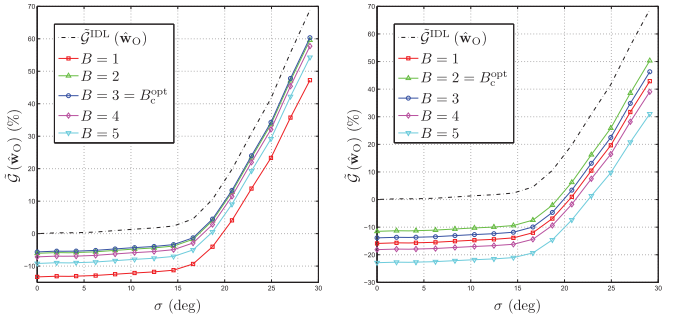

(a) $M_I = 3$ and $\bar{f}_{\mathrm{D}} = 0.0001$.

(b) $M_I = 3$ and $\bar{f}_{\mathrm{D}} = 0.0002$.

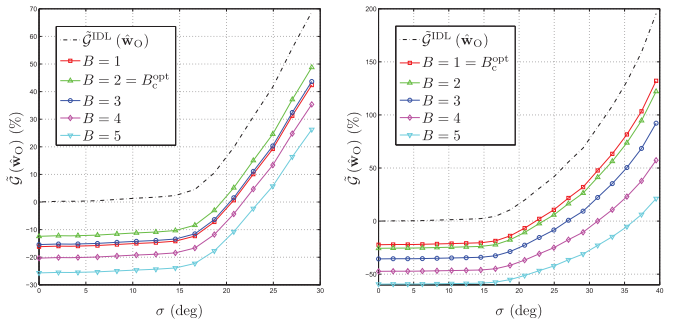

(c) $M_I = 5$ and $\bar{f}_{\mathrm{D}} = 0.0001$.

(d) $M_I = 5$ and $\bar{f}_{\mathrm{D}} = 0.0002$.

Fig. 4. The throughput gain $\tilde{\mathcal{G}}(\hat{\mathbf{w}}_{\mathrm{O}})$ achieved by OCB versus σ for different values of $\bar{f}_{\mathrm{D}}$, M_I, and B_{c}.

the empirical $\hat{\Upsilon}(\hat{\mathbf{w}}_{\mathrm{M}})$ and $\hat{\Upsilon}(\hat{\mathbf{w}}_{\mathrm{O}})$, respectively, for $K = 20$. It can be observed from Fig. 3(a) that $\hat{\Upsilon}(\hat{\mathbf{w}}_{\mathrm{M}}) \simeq 1$ holds regardless B_{a} when $\sigma = 0$ (i.e., there is no scattering). However, when $\sigma \neq 0$, $\hat{\Upsilon}(\hat{\mathbf{w}}_{\mathrm{M}})$ increases if the quantization level B_{a} decreases and even slightly exceeds 1 when B_{a} becomes very small (i.e., $B_{\mathrm{a}} \leq 3$). Therefore, under real-world conditions, the proposed B-DCB always outperforms MCB except at unrealistic low quantization levels which are hard to justify in practice. This corroborates the discussions made in Section VI-A1. As discussed in Section VI-A2, from Fig. 3(b), the ASAINR gain $\hat{\Upsilon}(\hat{\mathbf{w}}_{\mathrm{O}})$ achieved by OCB against the proposed B-DCB decreases with $\bar{f}_{\mathrm{D}}$. This figure confirms and illustrates the existence of a threshold value of $\bar{f}_{\mathrm{D}}$ beyond which the ASAINR gain achieved by OCB turns into losses. As expected, this threshold whose expression is given by (57) increases with σ, since $\tilde{\xi}_{\hat{\mathbf{w}}_{\mathrm{BD}}}$ decreases with the latter. For instance, we find that $\hat{\Upsilon}(\hat{\mathbf{w}}_{\mathrm{O}}) \leq 1$ when $\sigma = 20$ degrees if $\bar{f}_{\mathrm{D}} \geq 0.025$ or when $\sigma = 25$ degrees if $\bar{f}_{\mathrm{D}} \geq 0.087$.

Fig. 4 plots $\tilde{\mathcal{G}}\left(\hat{\mathbf{w}}_{\mathrm{O}}\right)$ versus σ for different values of $\bar{f}_{\mathrm{D}}$, M_I, and B_{c}. It also plots $\tilde{\mathcal{G}}^{\mathrm{IDL}}\left(\hat{\mathbf{w}}_{\mathrm{O}}\right)$, the throughput gain achieved by OCB against the proposed B-DCB under ideal conditions (i.e, without accounting for any overhead cost or any quantization or estimation error). From Figs. 4(a)-4(b), the OCB's throughput gain decreases, as discussed in Section VI-B1, not only with $\bar{f}_{\mathrm{D}}$ but also with the number of interfering sources M_I. From these figures, when σ is relatively small in lightly- to moderately-scattered environments, the proposed B-DCB always outperforms OCB in terms of achieved throughput. Actually, in such environments, their performances are almost equal only under idealistic conditions that ignore the practical effects of both overhead and estimation and quantization errors.

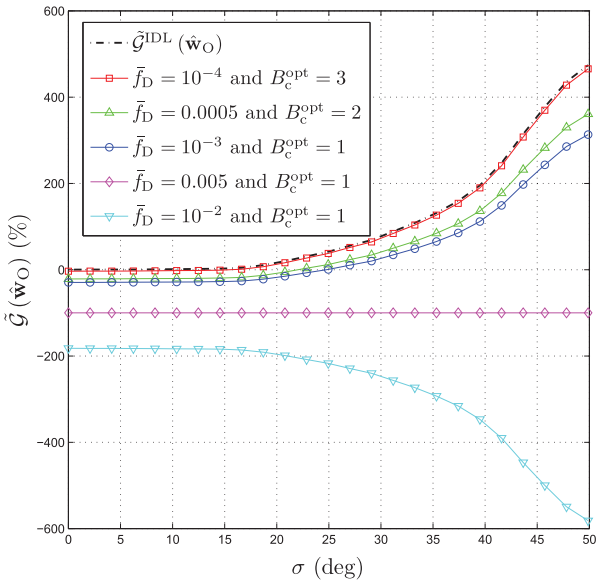

(a) $M_I = 3$ and $K = 20$.

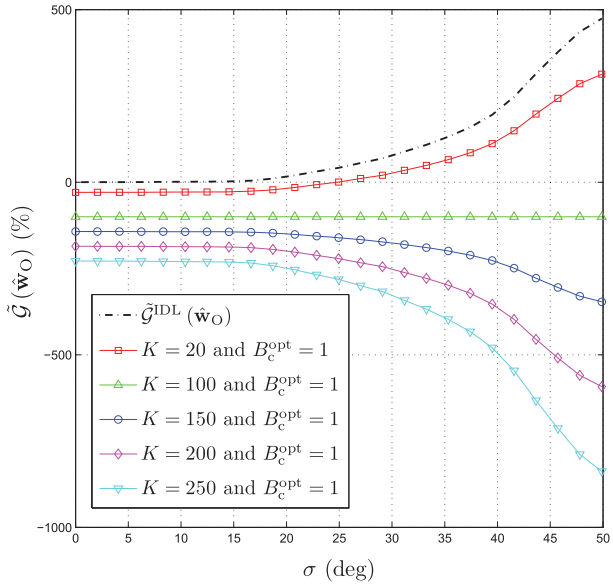

(b) $M_I = 3$ and $\bar{f}_{\mathrm{D}} = 0.001$.

Fig. 5. The throughput gain $\tilde{\mathcal{G}}(\hat{\mathbf{w}}_{\mathrm{O}})$ achieved by OCB versus σ for different values of $\bar{f}_{\mathrm{D}}$ and K.

Furthermore, we see from these figures that there exists an optimum quantization level $B_{\mathrm{c}}^{\mathrm{opt}}$ which maximizes the throughput (i.e., level that best minimizes combined losses due to errors and overhead) found to be equal to 3 and 1 at $\left(\bar{f}_{\mathrm{D}}, M_I\right)$ set to (0.0001, 3) and (0.0002, 5), respectively. At these levels, OCB suffers from throughput losses against the proposed B-DCB of about 6% and 22%, respectively, when σ is relatively small in lightly- to moderately-scattered environments. As can be observed from Fig. 4, these results translate into a larger operational region in terms of AS values over which the proposed B-DCB is favored against OCB. This operational region increases from about 15 degrees under ideal conditions to about 17 and 22 degrees, respectively in the two examples discussed above.

Fig. 5 displays $\tilde{\mathcal{G}}(\hat{\mathbf{w}}_{\mathrm{O}})$ for different values of $\bar{f}_{\mathrm{D}}$ and K. In this figure, curves are plotted after performing a numerical evaluation of the optimum quantization level $B_{\mathrm{c}}^{\mathrm{opt}}$ for each pair of values of $\bar{f}_{\mathrm{D}}$ and K. For instance, we find that $B_{\mathrm{c}}^{\mathrm{opt}}=2$ bits when $\bar{f}_{\mathrm{D}}=0.0005$ and $K=20$ while $B_{\mathrm{c}}^{\mathrm{opt}}=1$ bit when $\bar{f}_{\mathrm{D}}=10^{-3}$ and $K=200$. From this figure, the OCB's throughput gain against the proposed B-DCB decreases when $\bar{f}_{\mathrm{D}}$ and/or K increase/s. This gain may turn into losses for sufficiently large K and/or high $\bar{f}_{\mathrm{D}}$, even when σ is large. As can be observed from Fig. 5, this result translates into a larger operational region of up to 50 degrees for large K and/or high $\bar{f}_{\mathrm{D}}$ that amounts to angle deviations from almost -90 to 90 degrees (i.e., the entire angular span). Besides, $\tilde{\mathcal{G}}(\hat{\mathbf{w}}_{\mathrm{O}})$ which is nominally an increasing function of σ under ideal conditions, becomes constant at -100% when $K=20$ and $\bar{f}_{\mathrm{D}}=0.005$ or when $K=100$ and $\bar{f}_{\mathrm{D}}=0.001$, and even a decreasing function of σ, when K and/or $\bar{f}_{\mathrm{D}}$ are/is large. All these observations corroborate all the elements of our discussion in Section VI-B1.

VIII. Conclusions

In this paper, a dual-hop communication from a source surrounded by M_I interferences to a receiver was considered. In the first time slot, all sources send their signals to the network while, in the second time slot, the terminals multiply the received signal by their respective beamforming weights and forward the resulting signals to the receiver. These weights were designed so as to minimize the interferences plus noises' powers while maintaining the received power from the source to a constant level. We showed, however, that they are intractable in closed-form due to the complexity of the polychromatic channels arising from the presence of scattering. By resorting to a two-ray channel approximation proved valid at relatively low AS values, we were able to derive the new optimum weights and prove that they could be locally computed at each terminal, thereby complying with the distributed feature of the network of interest. The so-obtained B-DCB was then analyzed and compared in performance to both MCB, whose design does not account for scattering, and OCB. Comparisons were made under both ideal and real-world conditions where we accounted for implementation errors and the overhead incurred by each CB solution. They revealed that the proposed B-DCB always outperforms MCB in practice; and that it approaches OCB in lightly- to moderately-scattered environments under ideal conditions and outperforms it under real-world conditions even in highly-scattered environments. In such conditions, indeed, the B-DCB operational regions in terms of AS values over which it is favored against OCB could reach until 50 degrees and, hence, cover about the entire span of AS values.

Appendix A
Proof of Theorem 3

From (26), we have

$$\mathrm{E}\left\{\left|\mathbf{w}_{\mathrm{BD}}^{H}\mathbf{h}_m\right|^2\right\}=\frac{\mathrm{E}\{\eta_1\}+\mathrm{E}\{\eta_2\}+\mathrm{E}\left\{\eta_2^*\right\}+\mathrm{E}\{\eta_3\}}{K^2\left(1+2\frac{J_1(\gamma(2\sigma_1))}{\gamma(2\sigma_1)}-\boldsymbol{\nu}(\sigma_1)^T\mathbf{Q}^{-1}\boldsymbol{\nu}(\sigma_1)\right)^2},\tag{64}$$

where $\eta_1=\boldsymbol{\nu}(\sigma_1)^T\mathbf{Q}^{-1}\boldsymbol{\Gamma}^H\Sigma^{-1}\mathbf{h}_m\mathbf{h}_m^H\Sigma^{-1}\boldsymbol{\Gamma}\mathbf{Q}^{-1}\boldsymbol{\nu}(\sigma_1)$, $\eta_2=(\mathbf{a}(\sigma_\theta)+\mathbf{a}(-\sigma_\theta))^H\Sigma^{-1}\mathbf{h}_m\mathbf{h}_m^H\Sigma^{-1}\boldsymbol{\Gamma}\mathbf{Q}^{-1}\boldsymbol{\nu}(\sigma_1)$, and $\eta_3=(\mathbf{a}(\sigma_\theta)+\mathbf{a}(-\sigma_\theta))^H\Sigma^{-1}\mathbf{h}_m\mathbf{h}_m^H\Sigma^{-1}(\mathbf{a}(\sigma_\theta)+\mathbf{a}(-\sigma_\theta))$. Let us first focus on $\mathrm{E}\{\eta_3\}$. From assumption A1, we have

$$\begin{aligned}\mathrm{E}_{\alpha_{l,m}}\{\eta_1\}&=\sum_{l=1}^{L}\frac{1}{L}\left(\boldsymbol{\nu}(\sigma_1)^T\mathbf{Q}^{-1}\boldsymbol{\Gamma}^H\Sigma^{-1}\mathbf{a}\left(\phi_m+\theta_{l,m}\right)\right)\\&\quad\times\left(\mathbf{a}\left(\phi_m+\theta_{l,m}\right)^H\Sigma^{-1}\boldsymbol{\Gamma}\mathbf{Q}^{-1}\boldsymbol{\nu}(\sigma_1)\right)\\&=\sum_{l=1}^{L}\frac{1}{L}\left(\sum_{p=1}^{2M-2}\left[\boldsymbol{\nu}(\sigma_1)^T\mathbf{Q}^{-1}\right]_p\left[\mathbf{Q}^{-1}\boldsymbol{\nu}(\sigma_1)\right]_p\zeta_p\right.\\&\quad\left.+\sum_{p=1}^{2M-2}\sum_{n=1,n\neq p}^{2M-2}\left[\boldsymbol{\nu}(\sigma_1)^T\mathbf{Q}^{-1}\right]_p\left[\mathbf{Q}^{-1}\boldsymbol{\nu}(\sigma_1)\right]_n\delta_{p,n}\right),\end{aligned}\tag{65}$$

where $\zeta_p=\left[\boldsymbol{\Gamma}^H\Sigma^{-1}\mathbf{a}(\phi_m+\theta_{l,m})\right]_p\left[\mathbf{a}(\phi_m+\theta_{l,m})^H\Sigma^{-1}\boldsymbol{\Gamma}\right]_p$ and $\delta_{p,n}=\left[\boldsymbol{\Gamma}^H\Sigma^{-1}\mathbf{a}(\phi_m+\theta_{l,m})\right]_p\left[\mathbf{a}(\phi_m+\theta_{l,m})^H\Sigma^{-1}\boldsymbol{\Gamma}\right]_n$. ζ_p could be equivalently rewritten as

$$\begin{aligned}\zeta_p&=\left(\sum_{k=1}^{K}\frac{\left[\boldsymbol{\Gamma}^H\right]_{pk}\left[\mathbf{a}(\phi_m+\theta_{l,m})\right]_k}{[\Sigma]_{kk}}\right)\left(\sum_{s=1}^{K}\frac{\left[\mathbf{a}(\phi_m+\theta_{l,m})^H\right]_s[\boldsymbol{\Gamma}]_{sp}}{[\Sigma]_{ss}}\right)\\&=K+\sum_{k=1}^{K}e^{-j\gamma\left(\phi_m+\theta_{l,m}-\tilde{\phi}_p\right)\sin\left(\psi_k-\frac{\phi_m+\theta_{l,m}+\tilde{\phi}_p}{2}\right)}\\&\quad\times\sum_{s=1,s\neq k}^{K}e^{j\gamma\left(\phi_m+\theta_{l,m}-\tilde{\phi}_p\right)\sin\left(\psi_k-\frac{\phi_m+\theta_{l,m}+\tilde{\phi}_p}{2}\right)}.\end{aligned}\tag{66}$$

Using the fact that r_ks and ψ_ks are i.i.d random variables and $(2/\pi)\int_{-1}^{1}e^{j\gamma(\phi)z}\sqrt{1-z^2}dz=2J_1(\gamma(\phi))/\gamma(\phi)$, we show that

$$\mathrm{E}_{r_k,\psi_k}\{\zeta_p\}=K+2K(K-1)\left[\mathbf{z}\left(\phi_m+\theta_{l,m}\right)\right]_p\left[\mathbf{z}^T\left(\phi_m+\theta_{l,m}\right)\right]_p.\tag{67}$$

We also show that

$$\begin{aligned}\mathrm{E}_{\alpha_{l,m},r_k,\psi_k}\{\delta_{p,n}\}&=2K[\mathbf{Q}]_{pq}+2K(K-1)\left[\mathbf{z}\left(\phi_m+\theta_{l,m}\right)\right]_p\\&\quad\times\left[\mathbf{z}^T\left(\phi_m+\theta_{l,m}\right)\right]_n.\end{aligned}\tag{68}$$

It follows then from (67) and (68) that

$$\begin{aligned}\mathrm{E}_{\alpha_{l,m},r_k,\psi_k}\{\eta_1\}&=\sum_{l=1}^{L}\frac{1}{L}\left(2K\boldsymbol{\nu}(\sigma_1)^T\mathbf{Q}^{-1}\boldsymbol{\nu}(\sigma_1)\right.\\&\quad\left.+4K(K-1)\left(\mathbf{z}^T\left(\phi_m+\theta_{l,m}\right)\mathbf{Q}^{-1}\boldsymbol{\nu}(\sigma_1)\right)^2\right),\end{aligned}\tag{69}$$

since $[\mathbf{Q}]_{pp}=1/2$. Furthermore, following the same approach above, we prove that

$$\mathrm{E}_{\alpha_{l,m},r_k,\psi_k}\{\eta_2\} = \sum_{l=1}^{L}\frac{1}{L}\left(2K\boldsymbol{\nu}(\sigma_1)^T\mathbf{Q}^{-1}\boldsymbol{\nu}(\sigma_1) + 4K(K-1)\right.$$
$$\times\left(\frac{J_1\left(\gamma\left(\phi_m+\theta_{l,m}+\sigma_1\right)\right)}{\gamma\left(\phi_m+\theta_{l,m}+\sigma_1\right)}\right.$$
$$\left.\left.+\frac{J_1\left(\gamma\left(\phi_m+\theta_{l,m}-\sigma_1\right)\right)}{\gamma\left(\phi_m+\theta_{l,m}-\sigma_1\right)}\right)\mathbf{z}^T\left(\phi_m+\theta_{l,m}\right)\mathbf{Q}^{-1}\boldsymbol{\nu}(\sigma_1)\right), \tag{70}$$

and

$$\mathrm{E}_{\alpha_{l,m},r_k,\psi_k}\{\eta_3\} = \sum_{l=1}^{L}\frac{1}{L}\left(2K\boldsymbol{\nu}(\sigma_1)^T\mathbf{Q}^{-1}\boldsymbol{\nu}(\sigma_1) + 4K(K-1)\right.$$
$$\left.\times\left(\frac{J_1\left(\gamma\left(\phi_m+\theta_{l,m}+\sigma_1\right)\right)}{\gamma\left(\phi_m+\theta_{l,m}+\sigma_1\right)}+\frac{J_1\left(\gamma\left(\phi_m+\theta_{l,m}-\sigma_1\right)\right)}{\gamma\left(\phi_m+\theta_{l,m}-\sigma_1\right)}\right)^2\right). \tag{71}$$

Note that $\mathrm{E}_{\alpha_{l,m},r_k,\psi_k}\{\eta_2\} = \mathrm{E}_{\alpha_{l,m},r_k,\psi_k}\left\{\eta_2^*\right\}$ since $\mathrm{E}_{r_k,\psi_k}\{\eta_2\}$ is real. Finally, applying the expectation with respect to $\theta_{l,m}$s over both sides of (69)–(71) and substituting the resulting equations in (64), $\mathrm{E}\left\{\left|\mathbf{w}_{\mathrm{BD}}^H\mathbf{h}_m\right|^2\right\}$ is obtained for $m = 1,\ldots,M$. On the other hand, it can be shown that

$$\mathrm{E}\left\{\mathbf{w}_{\mathrm{BD}}^H\Sigma\mathbf{w}_{\mathrm{BD}}\right\} = \frac{2}{K\left(1+2\frac{J_1(\gamma(2\sigma_1))}{\gamma(2\sigma_1)}-\boldsymbol{\nu}(\sigma_1)^T\mathbf{Q}^{-1}\boldsymbol{\nu}(\sigma_1)\right)}. \tag{72}$$

Using $\mathrm{E}\left\{\left|\mathbf{w}_{\mathrm{BD}}^H\mathbf{h}_m\right|^2\right\}$ along with the latter result, we obtain the expression of $\tilde{\xi}_{\mathbf{w}_{\mathrm{BD}}}$.

Appendix B
Proof of Theorem 4

It follows from (30) that

$$\lim_{K\to\infty}\tilde{\xi}_{\mathbf{w}_{\mathrm{M}}} = \frac{p_1\mathrm{E}\left\{\lim_{K\to\infty}\left|\mathbf{w}_{\mathrm{M}}^H\mathbf{h}_1\right|^2\right\}}{\sum_{m=2}^{M}p_m\mathrm{E}\left\{\lim_{K\to\infty}\left|\mathbf{w}_{\mathrm{M}}^H\mathbf{h}_m\right|^2\right\}+\sigma_{n_t}^2\mathrm{E}\left\{\lim_{K\to\infty}\mathbf{w}_{\mathrm{M}}^H\Sigma\mathbf{w}_{\mathrm{M}}\right\}+\sigma_{n_r}^2}. \tag{73}$$

Using the matrix inversion lemma to break the matrix $\left(\mathbf{A}_{\bar{1}}\mathbf{P}_{\bar{1}}\mathbf{A}_{\bar{1}}^H+\sigma_{n_t}^2\Sigma\right)^{-1}$ into several terms yields

$$\mathbf{w}_{\mathrm{M}}^H\mathbf{h}_m = \frac{\mathbf{a}(0)^H\Sigma^{-1}\mathbf{h}_m-\mathbf{a}(0)^H\Sigma^{-1}\mathbf{A}_{\bar{1}}\left(\mathbf{A}_{\bar{1}}\mathbf{P}_{\bar{1}}\mathbf{A}_{\bar{1}}^H\right)^{-1}\mathbf{A}_{\bar{1}}^H\Sigma^{-1}\mathbf{h}_m}{K-\mathbf{a}(0)^H\Sigma^{-1}\mathbf{A}_{\bar{1}}\left(\mathbf{A}_{\bar{1}}\mathbf{P}_{\bar{1}}\mathbf{A}_{\bar{1}}^H\right)^{-1}\mathbf{A}_{\bar{1}}^H\Sigma^{-1}\mathbf{a}(0)^H}, \tag{74}$$

for $m = 1,\ldots,M$. Moreover, it follows from Theorem 1 that $\frac{\mathbf{a}(0)^H\Sigma^{-1}\mathbf{h}_m}{K}\xrightarrow{p1}2\sum_{l=1}^{L}\alpha_{l,m}\frac{J_1(\gamma(\phi_m+\theta_{l,m}))}{\gamma(\phi_m+\theta_{l,m})}$, $\frac{\mathbf{A}_{\bar{1}}^H\Sigma^{-1}\mathbf{a}(0)}{K}\xrightarrow{p1}2\boldsymbol{\nu}_{\mathrm{M}}(0)$, $\frac{\mathbf{A}_{\bar{1}}\mathbf{P}_{\bar{1}}\mathbf{A}_{\bar{1}}^H}{K}\xrightarrow{p1}2\mathbf{Q}_{\mathrm{M}}$, and $\frac{\mathbf{A}_{\bar{1}}^H\Sigma^{-1}\mathbf{h}_m}{K}\xrightarrow{p1}2\sum_{l=1}^{L}\alpha_{l,m}\boldsymbol{\nu}_{\mathrm{M}}(\phi_m+\theta_{m,l})$ when $K\to\infty$. Using these results in (74), we obtain for large K

$$\left|\mathbf{w}_{\mathrm{M}}^H\mathbf{h}_m\right|^2\xrightarrow{p1}\frac{4\left|\sum_{l=1}^{L}\alpha_{l,m}\left(\frac{J_1(\gamma(\phi_m+\theta_{l,m}))}{\gamma(\phi_m+\theta_{l,m})}-\boldsymbol{\nu}_{\mathrm{M}}^T(0)\mathbf{Q}_{\mathrm{M}}^{-1}\boldsymbol{\nu}_{\mathrm{M}}(\phi_m+\theta_{l,m})\right)\right|^2}{1-2\boldsymbol{\nu}_{\mathrm{M}}^T(0)\mathbf{Q}_{\mathrm{M}}^{-1}\boldsymbol{\nu}_{\mathrm{M}}(0)}. \tag{75}$$

On the other hand, following similar steps as above, one could easily show that $\lim_{K\to\infty}\mathbf{w}_{\mathrm{M}}^H\Sigma\mathbf{w}_{\mathrm{M}} = 0$. Furthermore, it can be inferred from (75) that

$$\mathrm{E}_{\alpha_{l,m}}\left\{\left|\mathbf{w}_{\mathrm{M}}^H\mathbf{h}_m\right|^2\right\} = \frac{4\left(\frac{J_1(\gamma(\phi_m+\theta_{l,m}))}{\gamma(\phi_m+\theta_{l,m})}-\boldsymbol{\nu}_{\mathrm{M}}^T(0)\mathbf{Q}_{\mathrm{M}}^{-1}\boldsymbol{\nu}_{\mathrm{M}}(\phi_m+\theta_{l,m})\right)^2}{1-2\boldsymbol{\nu}_{\mathrm{M}}^T(0)\mathbf{Q}_{\mathrm{M}}^{-1}\boldsymbol{\nu}_{\mathrm{M}}(0)}. \tag{76}$$

Note that we resort to assumption A1 in (76). Applying the expectation with respect to $\theta_{l,m}$s over both sides of (76) yields $\mathrm{E}\left\{\left|\mathbf{w}_{\mathrm{M}}^H\mathbf{h}_m\right|^2\right\} = 4\Psi_{\mathrm{M}}(\phi_m)/(1-2\boldsymbol{\nu}_{\mathrm{M}}^T(0)\mathbf{Q}_{\mathrm{M}}^{-1}\boldsymbol{\nu}_{\mathrm{M}}(0))$ and, therefore, (35) is obtained.

Appendix C
Proof of Theorem 5

It is straightforward to show from (28) that $\mathbf{w}_{\mathrm{O}}^H\mathbf{h}_1 = 1$. However, $\mathbf{w}_{\mathrm{O}}^H\mathbf{h}_m$ is given by

$$\mathbf{w}_{\mathrm{O}}^H\mathbf{h}_m = \frac{\mathbf{h}_1^H\Sigma^{-1}\mathbf{h}_m-\mathbf{h}_1^H\Sigma^{-1}\mathbf{H}_{\bar{1}}\left(\mathbf{H}_{\bar{1}}\mathbf{P}_{\bar{1}}\mathbf{H}_{\bar{1}}^H+\sigma_{n_t}^2\Sigma\right)^{-1}\mathbf{H}_{\bar{1}}^H\Sigma^{-1}\mathbf{h}_m}{\mathbf{h}_1^H\Sigma^{-1}\mathbf{h}_1-\mathbf{h}_1^H\Sigma^{-1}\mathbf{H}_{\bar{1}}\left(\mathbf{H}_{\bar{1}}\mathbf{P}_{\bar{1}}\mathbf{H}_{\bar{1}}^H+\sigma_{n_t}^2\Sigma\right)^{-1}\mathbf{H}_{\bar{1}}^H\Sigma^{-1}\mathbf{h}_1}, \tag{77}$$

for $m = 2,\ldots,M$. On the other hand, exploiting the strong law of large numbers and assumption A1, we show for large L_1 that $\frac{\mathbf{h}_1^H\Sigma^{-1}\mathbf{h}_1}{L_1}\xrightarrow{p1}\frac{K}{L_1}$, $\frac{\mathbf{h}_1^H\Sigma^{-1}\mathbf{h}_m}{L_1}\xrightarrow{p1}0$, and $\frac{\mathbf{H}_{\bar{1}}^H\Sigma^{-1}\mathbf{h}_1}{L_1}\xrightarrow{p1}0$. It follows from these results that $\mathbf{w}_{\mathrm{O}}^H\mathbf{h}_m\xrightarrow{p1}0$ for $m = 2,\ldots,M$. Furthermore, using the latter results, we prove for large L_1 that $\mathbf{w}_{\mathrm{O}}^H\Sigma\mathbf{w}_{\mathrm{O}}\xrightarrow{p1}K$ and, therefore, (41) is obtained.

References

[1] Y. Jing and H. Jafarkhani, "Network beamforming using relays with perfect channel information," *IEEE Trans. Inf. Theory*, vol. 55, no. 6, pp. 2499–2517, Jun. 2009.

[2] H. Shen, W. Xu, S. Jin, and C. Zhao, "Joint transmit and receive beamforming for MIMO downlinks with channel uncertainty," *IEEE Trans. Veh. Tech.*, vol. 63, no. 5, pp. 2319–2335, Jun. 2014.

[3] H.-B. Kong, C. Song, H. Park, and I. Lee, "A new beamforming design for MIMO AF relaying systems with direct link," *IEEE Trans. Commun.*, vol. 62, no. 7, pp. 2286–2295, Jul. 2014.

[4] Z. Yi and I. Kim, "Joint optimization of relay-precoders and decoders with partial channel side information in cooperative networks," *IEEE J. Sel. Areas Commun.*, vol. 25, no. 2, pp. 447–458, Feb. 2007.

[5] V. Havary-Nassab, S. Shahbazpanahi, A. Grami, and Z.-Q. Luo, "Distributed beamforming for relay networks based on second-order statistics of the channel state information," *IEEE Trans. Signal Process.*, vol. 56, no. 9, pp. 4306–4316, Sep. 2008.
[6] L. C. Godara, "Application of antenna arrays to mobile communications, Part II: Beam-forming and direction-of-arrival considerations," *Proc. IEEE*, vol. 85, pp. 1195–1245, Aug. 1997.
[7] R. Mudumbai, G. Barriac, and U. Madhow, "On the feasibility of distributed beamforming in wireless networks," *IEEE Trans. Wireless Commun.*, vol. 6, no. 5, pp. 1754–1763, May 2007.
[8] R. Mudumbai, D. R. Brown, U. Madhow, and H. V. Poor, "Distributed transmit beamforming: Challenges and recent progress," *IEEE Commun. Mag.*, vol. 47, no. 2, pp. 102–110, Feb. 2009.
[9] M. Zeng, R. Zhang, and S. Cui, "On design of collaborative beamforming for two-way relay networks," *IEEE Trans. Signal Process.*, vol. 59, no. 5, pp. 2284–2295, May 2011.
[10] S. Zaidi and S. Affes, "SNR and throughput analysis of distributed collaborative beamforming in locally-scattered environments," *Wiley J. Wireless Commun. Mobile Comput.*, vol. 12, pp. 1620–1633, Dec. 2012, invited paper.
[11] S. Zaidi and S. Affes, "Analysis of collaborative beamforming designs in real-world environments," in *Proc. IEEE Wireless Commun. Netw. Conf. (WCNC'13)*, Shanghai, China, Apr. 7–10, 2013.
[12] H. Ochiai, P. Mitran, H. V. Poor, and V. Tarokh, "Collaborative beamforming for distributed wireless ad hoc sensor networks," *IEEE Trans. Signal Process.*, vol. 53, no. 11, pp. 4110–4124, Nov. 2005.
[13] M. F. A. Ahmed and S. A. Vorobyov, "Collaborative beamforming for wireless sensor networks with Gaussian distributed sensor nodes," *IEEE Trans. Wireless Commun.*, vol. 8, no. 2, pp. 638–643, Feb. 2009.
[14] J. Huang, P. Wang, and Q. Wan, "Collaborative beamforming for wireless sensor networks with arbitrary distributed sensors," *IEEE Commun. Lett.*, vol. 16, no. 7, pp. 1118–1120, Jul. 2012.
[15] K. Zarifi, A. Ghrayeb, and S. Affes, "Distributed beamforming for wireless sensor networks with improved graph connectivity and energy efficiency," *IEEE Trans. Signal Process.*, vol. 58, no. 3, pp. 1904–1921, Mar. 2010.
[16] M. F. A. Ahmed and S. A. Vorobyov, "Sidelobe control in collaborative beamforming via node selection," *IEEE Trans. Signal Process.*, vol. 58, no. 12, pp. 6168–6180, Dec. 2010.
[17] Z. Han and H. V. Poor, "Lifetime improvement in wireless sensor networks via collaborative beamforming and cooperative transmission," *IET Microw. Antennas Propag.*, vol. 1, no. 6, pp. 1103–1110, Dec. 2007.
[18] L. Dong, A. P. Petropulu, and H. V. Poor, "A cross-layer approach to collaborative beamforming for wireless ad hoc networks," *IEEE Trans. Signal Process.*, vol. 56, no. 7, pp. 2981–2993, Jul. 2008.
[19] A. Amar, "The effect of local scattering on the gain and beamwidth of a collaborative beampattern for wireless sensor networks," *IEEE Trans. Wireless Commun.*, vol. 9, no. 9, pp. 2730–2736, Sep. 2010.
[20] S. Zaidi and S. Affes "Distributed collaborative beamforming in the presence of angular scattering," *IEEE Trans. Commun.*, vol. 62, no. 5, pp. 1668–1680, May 2014.
[21] S. Zaidi and S. Affes, "Distributed beamforming for wireless sensor networks in local scattering environments," *Proc. IEEE Veh. Technol. Conf. (VTC'12-Fall)*, Québec City, Canada, Sep. 3–6, 2012.
[22] S. Zaidi and S. Affes, "Distributed collaborative beamforming with minimum overhead for local scattering environments," in *Proc. IEEE 8th Int. Wireless Commun. Mobile Comput. Conf. (IWCMC'12)*, Cyprus, Aug. 27–31, 2012, invited paper.
[23] K. Zarifi, S. Zaidi, S. Affes, and A. Ghrayeb, "A distributed amplify-and-forward beamforming technique in wireless sensor networks," *IEEE Trans. Signal Process.*, vol. 59, no. 8, pp. 3657–3674, Aug. 2011.
[24] K. Zarifi, S. Affes, and A. Ghrayeb, "Collaborative null-steering beamforming for uniformly distrubuted wireless sensor networks," *IEEE Trans. Signal Process.*, vol. 58, no. 3, pp. 1889–1903, Mar. 2010.
[25] D. J. Love, R. W. Heath, and T. Strohmer, "Grassmannian beamforming for multiple-input multiple-output wireless systems," *IEEE Trans. Inf. Theory*, vol. 49, no. 10, pp. 2735–2747, Oct. 2003.
[26] D. Astly and B. Ottersten, "The effects of local scattering on direction of arrival estimation with MUSIC," *IEEE Trans. Signal Process.*, vol. 47, no. 12, pp. 3220–3234, Dec. 1999.
[27] M. Bengtsson and B. Ottersten, "Low-complexity estimators for distributed sources," *IEEE Trans. Signal Process.*, vol. 48, no. 8, pp. 2185–2194, Aug. 2000.
[28] M. Souden, S. Affes, and J. Benesty, "A two-stage approach to estimate the angles of arrival and the angular spreads of locally scattered sources," *IEEE Trans. Signal Process.*, vol. 56, no. 5, pp. 1968–1983, May 2008.
[29] S. Zaidi, B. Hmidet, and S. Affes, "Power-constrained distributed implementation of SNR-optimal collaborative beamforming in highlyscattered environments," *IEEE Wireless Commun., Lett.*, Vol. 4, no. 5, pp. 457–460, Oct. 2015.
[30] S. Zaidi and S. Affes, "Distributed collaborative beamforming design for maximized throughput in real-world environments," in *Proc. IEEE GLOBECOM'15*, San Diego, CA, USA, Dec. 6–10, 2015.
[31] S. Zaidi and S. Affes, "Spectrum-efficient distributed collaborative beamforming in the presence of local scattering and interference," in *Proc. IEEE GLOBECOM'12*, Anaheim, CA, USA, Dec. 3–7, 2012.
[32] B. D. Van Veen and K. M. Buckley, "Beamforming: A versatile approach to spatial filtering," *IEEE ASSP Mag.*, vol. 5, no. 2, pp. 4–24, Apr. 1988.
[33] S. Affes, S. Gazor, and Y. Grenier, "An algorithm for multisource beamforming and multitarget tracking," *IEEE Trans. Signal Process.*, vol. 44, no. 6, pp. 1512–1522, Jun. 1996.
[34] S. Zaidi and S. Affes, "Distributed collaborative beamforming design in scattered-environments," in *Proc. IEEE Int. Conf. Ubiq. Wireless Broadband (ICUWB'15)*, Montreal, Canada, Oct. 4–7, 2015.
[35] A. V. Oppenheim, R. W. Schafer, and J. R. Buck, *Discrete-Time Signal Processing*, 2nd ed. Englewood Cliffs, NJ, USA: Prentice-Hall, 1999.
[36] F. Bellili, S. B. Hassen, S. Affes, and A. Stéphenne, "Cramer-Rao lower bounds of DOA estimates from square QAM-modulated signals," *IEEE Trans. Signal Process.*, vol. 59, no. 6, pp. 1675–1685, Jun. 2011.
[37] S. Affes, P. Mermelstein, "Adaptive space-time Processing for wireless CDMA," in *Adaptive Signal Processing: Application to Real-World Problems*, J. Benesty, A. H. Huang, Eds. New York, NY, USA: Springer, Feb. 2003, ch. 10, pp. 283–321.
[38] M. K. Simon and M.-S. Alouini, *Digital Communications Over Fading Channels*. Hoboken, NJ, USA: Wiley, 2000.

Slim Zaidi received the B.Eng. degree in telecommunications from the National Engineering School of Tunis, Tunis, Tunisia, and the M.Sc. degree (with highest Hons.) from INRS, Montreal, QC, Canada, in 2008 and 2011, respectively. He is currently pursuing the Ph.D. degree at INRS. His research interests include statistical signal and array processing, MIMO, cooperative communications, millimeter wave communications, wireless sensor networks, mobile ad hoc networks, and cellular networks. He received twice the National Grant of Excellence from the Tunisian Government at both the M.Sc. (2009–2010) and the Ph.D. (2011–2013) programs. He also received a Top-Tier Graduate Ph.D. Scholarship from the Natural Sciences and Engineering Research Council (NSERC) of Canada (2013–2015). He had to decline another prestigious Ph.D. Scholarship offered over the same period from the "Fonds de Recherche du Québec Nature et Technologies" (FRQNT). Recently, Mr. Zaidi received a prestigious Postdoctoral Fellowship from FRQNT (2016–2018).

Sofiène Affes (SM'04) received the Diplôe d'Ingnieur degree in telecommunications and the Ph.D. degree (Hons.) in signal processing from École Nationale Suprieure des Télécommunications (ENST), Paris, France, in 1992 and 1995, respectively. He was a Research Associate with INRS, Montreal, QC, Canada, until 1997, an Assistant Professor, until 2000, and an Associate Professor, until 2009. Currently, he is a Full Professor and the Director of PERWADE, a unique $4 million research training program on wireless in Canada involving 27 faculty from 8 universities and 10 industrial partners. From 2003 to 2013, he was the Canada Research Chair in Wireless Communications. Currently, he is an Associate Editor for the IEEE TRANSACTIONS ON COMMUNICATIONS and the *Journal on Wireless Communications and Mobile Computing* (Wiley). He was previously an Associate Editor for the IEEE TRANSACTIONS ON WIRELESS COMMUNICATIONS and the IEEE TRANSACTIONS ON SIGNAL PROCESSING. He already served as a General Co-Chair of the IEEE VTC2006-Fall and the IEEE ICUWB 2015, both held in Montreal, QC, Canada. He was the recipient of the Discovery Accelerator Supplement Award (twice) from NSERC, from 2008 to 2011 and from 2013 to 2016, the Recognition Award from the IEEE Vehicular Technology Society in 2008, and a Certificate of Recognition from the IEEE Microwave Theory and Techniques Society in 2015.